Icarus 351 (2020) 113968

Contents lists available at ScienceDirect

Icarus

journal homepage: www.elsevier.com/locate/icarus

Dayside-to-nightside dust coma brightness asymmetry and its implications for nightside activity at comet 67P/Churyumov–Gerasimenko

S.-B. Gerig [a,*], O. Pinzón-Rodríguez [a], R. Marschall [b], J.-S. Wu [c], N. Thomas [a]

[a] Physikalisches Institut, University of Bern, Sidlerstrasse 5, 3012 Bern, Switzerland
[b] Southwest Research Institute, Boulder Office, 1050 Walnut St Suite 300, Boulder, CO 80302, USA
[c] Department of Mechanical Engineering, National Chiao Tung University, 1001 Ta-Hsueh Road, Hsinchu 30010, Taiwan

ARTICLE INFO

Keywords:
Rosetta
Simulation
Dust coma
Nightside activity

ABSTRACT

We have determined the dust coma brightness ratio between the dayside and the nightside (DS:NS) in OSIRIS images of comet 67P/Churyumov–Gerasimenko and compared them to results from numerical dust coma simulations to learn more about the dynamic processes that are involved in coma formation. The primary focus of this paper lies in the analysis of a subset of OSIRIS images acquired during one comet rotation on 11. April 2015 when the spacecraft was at a phase angle of 90° and therefore directly above the terminator. The DS:NS ratio was found to be 2.49 ± 0.18 on average - a very low value if insolation-driven sublimation of water dominates dust emission. We investigated two possible hypotheses: First, the influence of direct activity from non-illuminated (nightside) areas of the comet and second, the brightness contribution of large gravity-dominated particles in the innermost coma. For our numerical simulations, we used a combination of DSMC gas dynamics simulation and particle propagation by an equation of motion to simulate the dust coma. Our simulations show that direct activity from the nightside is preferred, contributing ≈ 10% of the total emission. We show that intensity profiles, used to quantify dust outflow behaviour, fit the observations better when nightside activity is present and we suggest that nightside gas emission by CO_2 or CO is responsible for the observed dust flux. With the help of a simplified Keplerian modelling approach we exclude large particles on gravitationally bound or ballistic orbits from being the major contributor to the observed dust coma brightness. Additionally, we show the DS:NS ratio as a function of days to perihelion and observe that it is on a similar level as in the April OSIRIS time series from February to mid-June 2015, but increases towards a maximum of ≥ 4.07± 0.49 shortly after perihelion passage. We suggest that this is correlated to the increasing importance of H_2O production when approaching perihelion.

1. Introduction

Cometary nuclei typically have diameters of a few kilometres. They consist of a mixture of refractory material, often referred to as dust, and ices. The most abundant volatile species on typical Jupiter-family comets (JFC) are water (H_2O), carbon dioxide (CO_2) and carbon monoxide (CO) (Le Roy et al., 2015). The sublimation of these frozen volatiles is the source of cometary activity, with the sublimating gases dragging dust from the surface into the inner coma. Comet 67P/Churyumov-Gerasimenko (67P) is a JFC and was the target of the European Space Agency's (ESA) cornerstone mission, *Rosetta*. The *Rosetta* spacecraft reached 67P in August 2014 and escorted it along its orbit for about two years through perihelion and beyond until the mission ended in September 2016. Among the scientific instruments, the Optical, Spectroscopic, and Infrared Remote Imaging System (OSIRIS) narrow-angle camera (NAC) and wide-angle camera (WAC) provided images in the visible spectral range (240–1000 nm) (Keller et al., 2007) to monitor continuously the nucleus surface and dust coma. The dust coma surrounding the nucleus is mainly driven by insolation-induced sublimation of volatiles from surface or near-surface ices and can be directly observed on OSIRIS images through the sunlight that is scattered by dust particles in the coma. Most of the images show a diffuse global dust coma with distinct jet-like structures. Gas contributions to the brightness of the coma observed in its broad-band filters by OSIRIS are negligible. However, the coma structures arise from a complex combination of the irregular surface morphology and an inhomogeneous gas source distribution over the surface of the nucleus. Determining the source distribution of the gas has been the subject of previous extensive studies (e.g. Fougere et al., 2016; Marschall et al., 2016; Zakharov et al., 2018a; Combi et al., 2020).

* Corresponding author.
E-mail address: selina-barbara.gerig@space.unibe.ch (S.-B. Gerig).

https://doi.org/10.1016/j.icarus.2020.113968
Received 18 December 2019; Received in revised form 16 June 2020; Accepted 3 July 2020
Available online 6 July 2020

In this paper we focus on the brightness distribution of the innermost diffuse dust coma out to distances of 10–20 km above the illuminated dayside and the non-illuminated nightside as observed in projection by the 2D imaging system. We define the dayside-to-nightside dust coma brightness ratio (DS:NS) as the ratio between the averaged brightness on the dayside and the nightside coma at a distance of 10 to 12 km. We study this particular coma characteristic in OSIRIS images and artificial images from numerical simulations with the aim to gain new insight into the dynamic processes governing the innermost dust coma. In a perfect case, an observation from directly above the terminator gives exactly the dust brightness above each hemisphere. When the phase angle is not 90°, the DS:NS ratio is affected by projection effects in 2D line-of-sight data. Hence, we select and analyse images specifically for 90° phase angle geometry.

The simplest model of cometary outflow is to assume force-free radial expansion from a spherical nucleus emitting only from the dayside. In this approximation, one would expect a very high DS:NS ratio for phase angles close to 90° (for a phase angle of exactly 90° the DS:NS ratio would be infinite). The ejected dust is moving outwards with constant speed and the dust column density, which is proportional to the brightness observed by a line-of-sight instrument such as the OSIRIS cameras, is decreasing with the inverse of the distance to the source centre. In cometary literature this is often referred to as the $1/r$-law and we will use the same notation in this paper when referring to this specific relation. In reality, comets are more complex systems. Shape effects of the irregular nucleus considerably influence the dust outflow in the first few kilometres above the surface and the dust motion is by no means force-free. The two dominant forces governing dust outflow dynamics in the innermost coma are the drag force that gas exerts on dust particles and the comet's gravitational force. The acceleration of dust particles through gas drag leads to a deviation from $1/r$ towards steeper slopes close to the nucleus similar to that observed for 67P (Gerig et al., 2018).

Already in 1989, the dayside coma of comet 1P/Halley was noticed to be only 3.2 times brighter than the nightside coma from images taken by the Halley Multicolour Camera during the fly-by of the *Giotto* spacecraft at a phase angle of 107° and a heliocentric distance of 0.89 AU (Keller and Thomas, 1989). Such a low DS:NS coma brightness ratio was quite unexpected. It was interpreted by Keller and Thomas (1989) to be the consequence of near-surface lateral transport caused by gas drag on dust from active regions towards the nightside, but no numerical simulations of this process were performed at the time. For 19P/Borrelly a DS:NS coma brightness ratio as low as 1.7 was found during the fly-by of the *Deep Space 1* spacecraft at a phase angle of 88° and a heliocentric distance of 1.36 AU (Ho et al., 2007). Again this is much lower than can be explained by insolation-driven emission and subsequent force-free radial outflow.

Here we attempt to determine the processes controlling the DS:NS ratio and model the influence of gravity-dominated particles and nightside activity to assess whether either of these mechanisms can match the observations. A significant number of large particles on bound or ballistic trajectories could noticeably change the observed coma brightness distribution by adding a significant flow from the dayside towards the nightside. The bound or ballistic particles falling back or orbiting above the nightside of the comet would add brightness to the nightside coma. Such particles were observed in the vicinity of 67P and are resolved in certain OSIRIS images (Fulle et al., 2015). Taking into account the resolution of the camera system, such particles have to be of the order of centimetres to metres in size and are slow moving with respect to the nucleus with most close to or below escape velocity. However, it is not well known how much these particles contribute in brightness to the unresolved coma we observe with the OSIRIS cameras.

In the last decades, numerical simulations have proven to be an increasingly important tool to interpret and predict observations of gas and dust comae around comets. Most gas dynamics calculations of cometary outgassing include some form of uniform outgassing from the nightside at production rates equivalent to 2%–10% of the total production rate. Bieler et al. (2015), for example, used 7%–10% to match ROSINA Comet Pressure Sensor (COPS) data between August 2014 and January 2015 at 67P. Marschall et al. (2016) deliberately did not include gas activity on the nightside but their fitting to the COPS measurements noticeably underestimated the observed densities over the nightside and additional gas emission was clearly required. Outgassing directly from the nightside of the nucleus would also invoke nightside dust activity and could therefore be another reason for the increased coma brightness observed in OSIRIS images above the nightside. We note here that Bockelée-Morvan et al. (2015) found water production to be weak in regions with low solar illumination, but suggested that CO_2 is outgassing from both illuminated and non-illuminated regions. It was suggested that this indicates that CO_2 sublimes from a depth that is below the diurnal skin depth. We shall show that this is indeed plausible.

In the following, we will present results from analysis of four OSIRIS images selected from a time series on 11. April 2015 and compare them with results from numerical simulations. In Section 2, we describe our data set, the methods we use for image analysis and present our results thereof. In particular, we focus on the DS:NS coma brightness ratio and the dust outflow profiles obtained using the "azimuthal average" (Gerig et al., 2018). In Section 3, we introduce our simulation methods and models. We give an overview of the DSMC model we use to simulate the gas coma and our dust dynamics simulation pipeline used to simulate the dust coma. We tested models with different activity source distributions over the surface and a model with added nightside activity. A more simplified modelling approach to simulate a background of large gravity dominated particles is also presented. In the results section (Section 4), we present and discuss the results of our numerical simulations and compare them to the findings from the OSIRIS image analysis. In the last section of this paper (Section 5), we summarise our results and conclude.

2. OSIRIS image analysis

2.1. Image subset for analysis

The analysed images form a subset of four OSIRIS images that were all acquired during one comet rotation on the 11. April 2015. Table 1 gives an overview of the properties of the analysed images. All images were taken with WAC filter 18 (Vis610; λ_c=612.6 nm central wavelength) and have an exposure time of 9.6 s. The heliocentric distance of the comet at the acquisition time was $D_\odot = 1.89AU$ and the spacecraft was at a distance of ≈141 km from the comet centre. The sun illuminated the nucleus at a latitude of about 10° north. The raw image data from the OSIRIS camera was corrected through the OSIRIS scientific calibration pipeline (OsiCalliope) (Tubiana et al., 2015). The calibration and correction pipeline includes corrections for analogue-to-digital converter (ADC) offset and gain, bias subtraction, high and low spatial frequency flat fielding, bad pixel and bad column removal, an exposure time normalisation, radiometric calibration and a correction for geometric distortion (resulting in CODMAC[1] level 4 data, in units of [$\mathrm{Wm^{-2}\ sr^{-1}\ nm^{-1}}$]). Images used in the data analysis presented in this paper (CODMAC level 4F) have additionally been corrected for out-of-field and in-field (ghost) stray light contributions and are transformed from radiometric units [$\mathrm{Wm^{-2}\ sr^{-1}\ nm^{-1}}$] into dimensionless reflectance units. The reflectance factor is defined as

$$R = \frac{\pi I(i, e, \alpha, \lambda)}{F(\lambda)} \tag{1}$$

with the observed spectral radiance I, the solar spectral irradiance at the corresponding heliocentric distance from the comet F, the incidence angle i, the emission angle e, the phase angle α, and the

[1] Committee On Data Management, Archiving and Computing (CODMAC) Data Level Definition (King and Greenstone, 1999, p. 34–35).

Table 1
List of the OSIRIS image file names from ESA's Planetary Science Archive (PSA) in the analysed image subset of the 11. April 2015. The observation timestamp, phase angle (α), sub-solar longitude (SSLong) and calculated DS:NS ratio are given as well.

No.	PSA file name	Timestamp	α [°]	SSLong [°]	DS:NS
A	W20150411T023758504ID4FF18	2015-04-11T02.37.58	89.66	46.26	2.46 ± 0.04
B	W20150411T050857774ID4FF18	2015-04-11T05.08.57	89.06	333.37	2.68 ± 0.03
C	W20150411T081257701ID4FF18	2015-04-11T08.12.57	88.33	244.54	2.56 ± 0.02
D	W20150411T120457516ID4FF18	2015-04-11T12.04.57	87.43	132.54	2.26 ± 0.02

wavelength λ. Note that the solar irradiance was calculated at the central wavelength of each filter. All calibration steps are described fully in the documentation of the pipeline which is available in the public domain on ESA's Planetary Science Archive (PSA) and can be found in the corresponding FTP data folders of the OSIRIS Wide Angle Camera (OSIWAC) instrument of the *Rosetta* mission under DOCUMENT/CALIB/OSIRIS_CAL_PIPELINE_V08.PDF. The selected images were acquired with the camera looking towards the dayside–nightside terminator at a phase angle close to 90°. This allows for a clear separation of the dayside (DS) and the nightside (NS) of the coma, because projection of radial dayside emission into the nightside is negligible. We refer to the projected coma above the illuminated side of the nucleus (± 90° from the sun azumithal angle in the image plane) as the dayside coma and, analogously, to the projected coma above the non-illuminated side of the nucleus as the nightside coma. The images were selected such that they cover the inner coma around the nucleus in every direction to a projected radial distance of more than 10 km. We refer to the projected distance from the centre of the nucleus in the image plane as the impact parameter, b.

2.2. Azimuthal average profiles

The basic idea of azimuthal average profiles ($\overline{Rb}$) is to visualise global outflow behaviour of cometary dust comae by showing brightness changes from flux integrations over quasi-closed surfaces. This method was introduced by Thomas and Keller (1990) in 1990 and they showed that cylindrical surfaces, realised as concentric circles in line-of-sight measurements such as camera images, are a good approximation for closed surfaces. In this paper we define the azimuthal average in terms of azimuthal angle ϕ as:

$$\overline{Rb} = \frac{b}{2\pi}\int_0^{2\pi} R(\phi, b)d\phi, \tag{2}$$

with R(ϕ, b) the image brightness as a function of azimuthal angle and impact parameter. To simplify interpretation of the profiles, the azimuthal average is often multiplied by the impact parameter, b, such that force-free radial outflow from a point source appears as a constant independent of distance to the centre of the source. This reflects the fact that column densities of radial outflow follows a $1/r$-law if the outflow is force-free. (With the definition of the impact parameter, b, we should in fact be talking about a "$1/b$-law" here, but to stay consistent with the cometary literature we will keep to the notation of "$1/r$-law" in this paper.) Any deviations of the azimuthal average profile from $1/r$-behaviour points towards additional physical processes acting on the dust in the coma. In Gerig et al. (2018) the application of azimuthal average profiles to *Rosetta* OSIRIS images is discussed in more detail. They showed in a comprehensive statistical study that the dust outflow behaviour beyond ≈12 km converges to force-free radial outflow in broad agreement with theoretical approximations described by Zakharov et al. (2018b). Additionally, possible processes at work in the inner coma of 67P and their effects on the azimuthal average were identified and discussed.

In Fig. 1(b), the azimuthal average profiles calculated for images A-D are shown. Every point in the profile corresponds to the averaged image brightness along a circle of constant b multiplied with the corresponding impact parameter. For the middle profile (black solid line) the brightness values were averaged over the full 360° angle (FA) range of the circle. The top black dash-dotted line profile corresponds to a brightness averaging over the dayside (DS) angle range (projected solar azimuth angle ± 90°) and the black dashed profile on the bottom of the diagram corresponds to the complementary brightness averaging over the nightside (NS) angle range. The dayside and the full angle profile show a decrease with distance close to the nucleus, which is dominated by the effects of the dust accelerating away from the surface (Gerig et al., 2018). The profile on the nightside is nearly constant indicating that the brightness is decreasing with the inverse of the impact parameter which is characteristic for a $1/r$-behaviour. This agrees well with radial dust profiles from observations with the Visible and InfraRed Thermal Imaging Spectrometer spectral mapping channel (VIRTIS-M; Coradini et al., 2007) on the 27. April 2015 as reported in Rinaldi et al. (2016), although we caution that radial profiles do not form closed surfaces and are therefore susceptible to error caused by non-radial expansion.

2.3. DS:NS coma brightness ratio

When looking at the images and profiles in Fig. 1, it is clear that the nightside coma is less bright than the dayside coma. This is expected for coma activity driven by dayside heat input with low thermal inertia as inferred by Groussin et al. (2019). To quantify the difference in brightness of the dayside to the nightside coma, we define the dayside-to-nightside coma brightness ratio (DS:NS). The ratio is calculated as

$$DS : NS = \frac{\int_{10\ \mathrm{km}}^{12\ \mathrm{km}} (\overline{Rb})_{DS} db}{\int_{10\ \mathrm{km}}^{12\ \mathrm{km}} (\overline{Rb})_{NS} db}, \tag{3}$$

with the subscripts DS and NS indicating the integration over the azimuthal average profiles over the dayside and nightside, respectively. The chosen distance range assures that we are comparing values in the region where the dust coma has nearly reached force-free radial outflow and where processes such as acceleration of the dust that dominate in the innermost <12 km above the nucleus surface have little influence on our result. We calculate an error for the DS:NS ratio by propagating the statistical errors from the averaging of the azimuthal average in the range between 10 and 12 km. The errors we find are very small (on the order of 1%). The ratio of DS:NS brightness in the selected OSIRIS image subset (Fig. 1) are given in Table 1. The average DS:NS ratio over the four OSIRIS images is 2.49 ± 0.18.

2.4. Solar radiation pressure reflected particles

To exclude that the observed night side diffuse activity is the result of dust density projection far from the nucleus into the OSIRIS line of sight we discuss the case of solar radiation pressure (SRP) reflected particles. Dust particle motion towards the Sun is reversed by SRP. Such SRP-reflected particles return into the near-nucleus field of view giving an almost constant background in images. This gives the first clear indication that the observed dust above the nightside is not the result of radiation pressure because Fig. 1 does not indicate a rise in $\overline{Rb}$ with distance on the nightside as would be expected for a constant background. In the OSIRIS images it can be observed that the nucleus is shadowing parts of the coma on the nightside leading to a brightness decrease of 11%–23% in the shadowed areas compared to the non-shadowed adjacent coma. To illustrate this we show the extremely

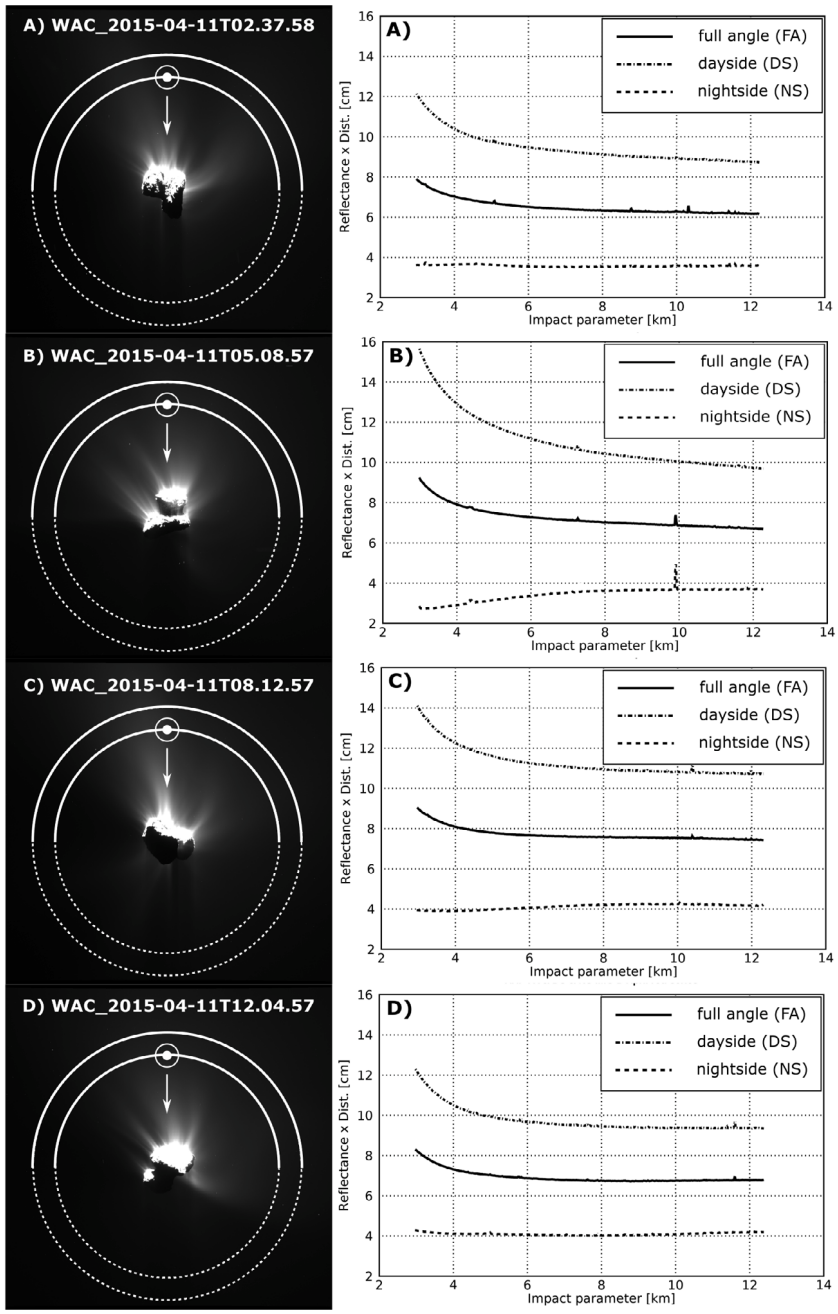

Fig. 1. (left) The brightness in images A-D from the April 2015 OSIRIS time series (Table 1) is stretched to make the faint coma visible ($R < 0.1 \cdot R_{max}$). The inner white circles mark a distance of 10 km and the outer white circles a distance of 12 km to the nucleus centre. The upper half (solid line) marks the dayside in the images and the lower half (dotted line) marks the nightside. The direction of the sun in the image planes is indicated by the arrows. (right) The corresponding azimuthal average profiles for the dayside (dashed-dot line), the full angle (solid line) and the nightside (dashed line) for images A-D (a) are shown.

stretched versions of images A-D in Fig. 2. The shadow cast by the nucleus onto the nightside coma is clearly visible. To verify that the measured brightness decrease lies in the range that would be expected from a shadowed near nucleus coma, we set up a simple theoretical model. The coma on the nightside more or less follows a 1/r-behaviour (Fig. 1) and we can therefore assume force-free radial outflow with constant velocity and write the local dust number densities as

$$n(r) = \frac{Q}{4\pi r^2 v}, \tag{4}$$

where Q is the dust production rate, v is the (constant) velocity of the outflow and r is the actual distance from a point source (Gerig et al., 2018). We further assume a spherical nucleus of radius $R_N = 2$ km and an observer at the distance of $d_{s/c}$ from the nucleus centre. A line-of-sight (LOS) integration through the coma lets us calculate column densities that are directly proportional to brightness values like OSIRIS would observe in an optically thin coma.

$$\int_{LOS} = \int_{-d_{s/c}}^{\infty} n(\vec{r})d\vec{r} - \left[\int_{-R_N}^{R_N} n(\vec{r})d\vec{r}\right]_{shadow} \tag{5}$$

We can estimate the decrease in brightness from the shadow cast by the nucleus on the coma without defining actual values for Q and v. The relative difference in brightness between a LOS integration at 10 km from the nucleus centre outside the nucleus shadow and a LOS integration at 10 km through the centre of the shadow is 12.8%. This lies well in the range of the brightness decrease measured in

the images. Different observation and illumination conditions on the complex nucleus and local inhomogeneities in the coma compared to force-free radial outflow can lead to the variations we observe. Hence, the brightness we observe on the nightside has to come from dust close to the nucleus to explain the decrease of brightness we observe in the nucleus shadow and cannot be dominated by particles in the far-field that are returned into the line of sight by SRP.

2.5. Considerations about image signal level

We also note that it is important to check that the analysed coma signal is well above the noise level of the image, especially for our nightside analysis. Long exposure images, like the ones we are using in this study, are especially suitable for analysis of weak coma signal because they generally provide a better signal-to-noise (S/N) ratio over the whole image. We calculated complete S/N maps for all four images in the April 2015 time series to estimate the image S/N level. We chose an approach following the description of the OSIRIS calibration steps in the documentation of the OSIRIS scientific calibration pipeline (DOCUMENT/CALIB/OSIRIS_CAL_PIPELINE_v08.PDF). We start with the raw data images (CODMAC level 2) in units of digital numbers (DN). In a first step, a correction for the ADC offset and gain (OSIRIS gain modes: high gain = 3.1 e^-/DN or low gain = 15.5 e^-/DN) is applied. The exact values used in the calculations for each image are taken from the calibration history header of the level 4F images. Then the image is corrected for bias by subtraction of the bias base value and the temperature dependent bias value. Finally, we apply a high and low frequency flat field correction by multiplication of the image matrix with the two corresponding flat field matrices. The corresponding file names can be found in the calibration history header under FLAT_HI_FILE and FLAT_LO_FILE and the corresponding flat field files are available publicly in the PSA. This results in image pixel (ij) signal values in number of electrons (S_{ij}) that are then used in the signal-to-noise calculation. The error for each pixel is a combination of the statistical Poisson error $E_p = \sqrt{S_{ij}}$, scaling with the number of detected electrons per pixel, and the coherent read-out-noise E_c of the detector. The values of the coherent read-out-noise for both cameras (NAC and WAC) can be found in the documentation of the calibration pipeline. In our calculations, we used the value of E_c (WAC) = 7.1 DN. Following the documentation of the calibration pipeline, the per-pixel error is then calculated in number of electrons as

$$\sigma_{ij} = \sqrt{E_c^2 + E_p^2}. \tag{6}$$

The S/N ratio is calculated by taking the ratio of the calculated signal level per pixel and the per-pixel error $(SNR)_{ij} = S_{ij}/\sigma_{ij}$. The resulting S/N maps are shown for all four images A-D on the right side in Fig. 2. The gradient in S/N ratio is depicted as colour contours and the signal-to-noise ratio is highest on the illuminated nucleus and around the sub-solar point in the dayside coma. The lowest S/N levels we reach on the nightside at distances between 10–12 km from the nucleus centre are in the range of 5–10, which ensures that we are working with real coma signal well above the camera noise level even when analysing the nightside where the coma signal is weaker than on the dayside. It is to be noted that, in general, we are summing many pixels to derive results and hence the actual S/N for our results are typically far higher.

3. Numerical simulations

We simulate rarefied gas outflow from the nucleus with the Direct Simulation Monte-Carlo method (DSMC; Bird and Brady, 1994) on the molecular level in 3D. In a second simulation step, we trace dust test particles through the calculated gas field and determine the dust number density distribution and the velocity of the flow in full 3D. In our simulation pipeline, the gas and dust coma simulations are completely decoupled, which means that we assume a gas dominated coma where the back-reaction of dust onto the gas is negligible. This is a good approximation if the energy transferred from the gas onto the dust is small of the order of a few percent as is the case in our simulations. Tenishev et al. (2011) also presented arguments that this is an adequate simplification.

In the next sections, we will outline our model pipeline in more detail. However, an in-depth description of the model can be found in Marschall et al. (2016).

3.1. Gas and dust dynamics simulation

3.1.1. DSMC

DSMC model setup. For modelling the gas outflow, we use a DSMC code called UltraSPARTS (ultra-fast Statistical PARTicle Simulation Package; www.plasmati.com.tw) It is a commercialised derivative of the code PDSC++ which was developed over the course of more than a decade to study rarefied gas dynamics under non-equilibrium conditions (Wu and Lian, 2003; Wu et al., 2004; Wu and Tseng, 2005; Su, 2013). In our simulations, we use the complex shape of the nucleus of 67P based on the SHAP7 shape model (Preusker et al., 2017) as the inlet boundary of the gas flow. We also simulate gas outflow from a spherical nucleus to study the effects in simplified geometries. For our simulations we use tetrahedron-based unstructured grids, which are generated using the Gridgen™ software by Pointwise® (www.pointwise.com/gridgen). The outer boundary of our simulation domain is spherical and located at a radius of 10 km from the nucleus centre. We calculate the solar incidence angle for every facet of the inlet surface for a specific illumination condition, including self-shadowing. The incidence angles determine the surface temperature through a thermal balance equation including sublimation of water ice. The calculated surface temperature is a lower limit, because we assume a pure ice surface in our calculations. On 67P however, ice on the surface has only been detected in specific locations as small icy patches (Pommerol et al., 2015) and is otherwise masked by dust which has a higher equilibrium temperature than sublimating ice. The sublimation rate for every inlet facet is calculated as a function of the surface temperature. At this stage, we simulate sublimation of just one gas species, namely H_2O. To scale the calculated production rates to match observed values, we introduce an effective active fraction (EAF) as a free parameter in our model. This parameter can be thought of as the fraction of the surface in percent that is effectively active. A completely icy surface would correspond to an EAF = 100. An EAF = 1 can therefore be interpreted as a surface that shows only 1% of the activity of that same surface completely covered with ice. We compare results from simulations with a homogeneous EAF over the whole comet with simulation results from simulations with a regionally inhomogeneous EAF (Fig. 3). In the case of a homogeneous EAF, approximately 2% of the total surface of the comet needs to be active in order to obtain a mean global gas production rate of 20 kg/s in the simulations, which corresponds to the total production rate calculated for 67P in April 2015 following the empirical interpolation of Hansen et al. (2016). In the case of a regionally inhomogeneous EAF we used different EAF values in different morphological regions (Thomas et al., 2015). We use the same regional EAF map that was found for Spring Equinox (May 2015) by Marschall et al. (2019), but scaled down to match the lower total production rates in April 2015.

A third model with a homogeneous EAF but with approximately 10% of the total activity in mass coming from the non-illuminated areas of the comet (including shadowed areas on the dayside) was tested. The exact fraction of activity from the non-illuminated surface facets changes slightly with illumination condition because the area of shadowed surface is not constant throughout a comet rotation due to the complex shape of the nucleus. Also in this case, we consider only outgassing of H_2O. To perform the simulation within our scheme, we have to increase the surface temperature on the nightside artificially to allow activity from those regions. The level of activity from the nightside as a first order estimate was determined through a trial

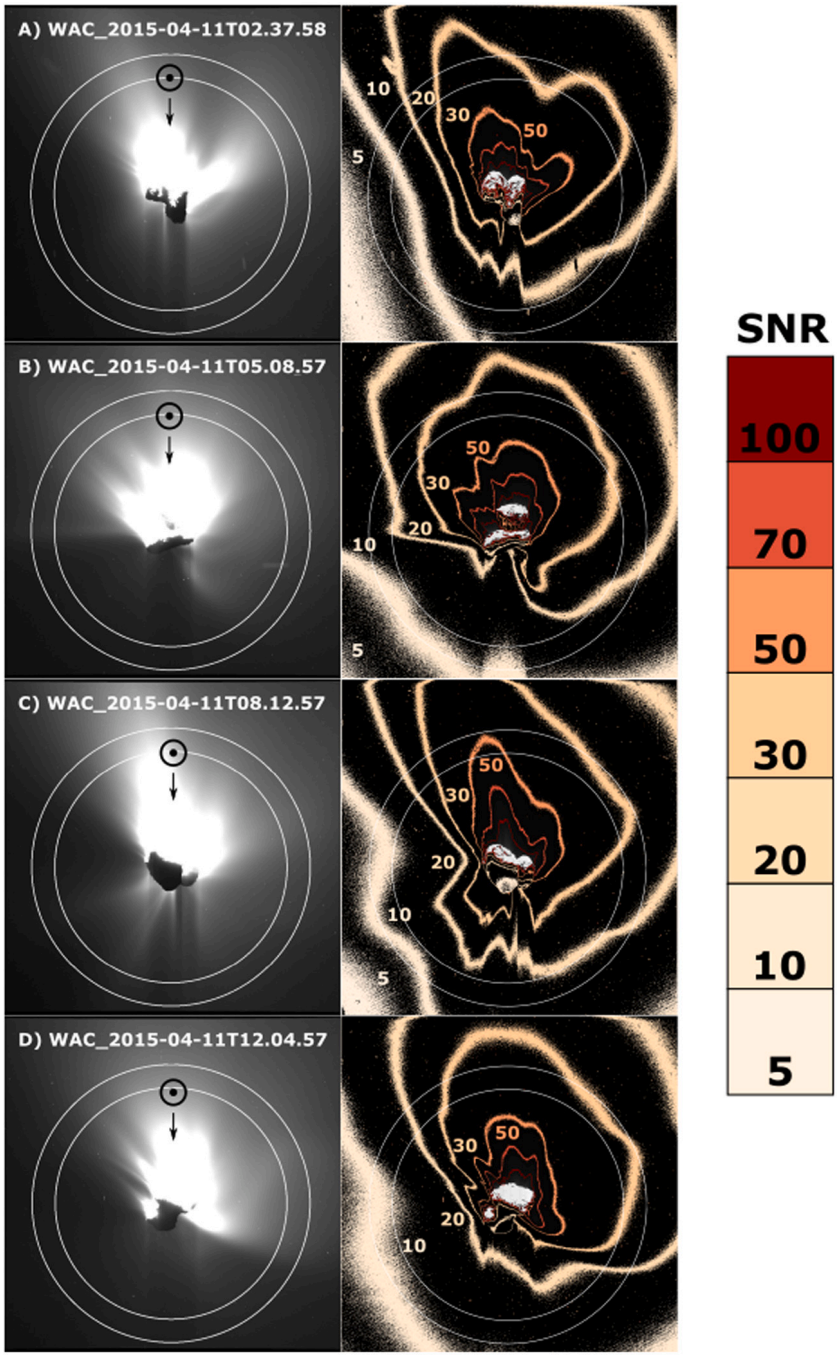

Fig. 2. (left) Images A-D stretched to the brightness range $[R_{min}, 0.02 \cdot R_{max}]$. The shadow the nucleus is casting on the nightside coma is visible in all four images, showing that the observed coma brightness on the nightside originates from light scattered by dust particles in the immediate vicinity of the nucleus. (right) Contour plot of images A-D showing the signal-to-noise ratio (SNR) in the coma around the nucleus. For orientation, the circles mark a distance of 10 km and 12 km from the nucleus centre in the image plane.

and error approach by step-wise increasing the artificial nightside temperature and with it activity from the nightside. To get about 10% of the global H_2O activity on the nightside, which provided the best fit to our data analysis, the shadowed model facets need to be at a temperature of 175 K. Such high temperatures are not expected on the nightside of comet 67P because the low thermal inertia values measured by *Rosetta* (e.g. MIRO: <80 J K^{-1} m^{-2} $s^{-0.5}$ for the Seth, Ash and Aten regions and VIRTIS: 40–160 K J K^{-1} m^{-2} $s^{-0.5}$ Marshall et al., 2018; or MUPUS locally at the Philae final landing site: 80 ± 35 J K^{-1} m^{-2} $s^{-0.5}$ Spohn et al., 2015) imply a rapid cooling of the surface once direct insolation stops. However, measurements of the near-surface brightness temperature by MIRO (Microwave Instrument for the *Rosetta* Orbiter; Gulkis et al., 2007) acquired in September 2014 for different effective latitudes on the nucleus indicate values between 100–160 K a few centimetres below the actual surface of the nucleus in non-illuminated areas (Schloerb et al., 2015). Accepting the brightness temperature as a proxy for the actual surface temperature, the surface on the nightside will be warm enough to maintain some activity, especially when taking into account more volatile gas species than H_2O, such as CO_2 or CO. They are more probable drivers of nightside dust activity on 67P (Bockelée-Morvan et al., 2015). A consistent model of CO_2 emission from the nightside will be addressed in more detail in a subsequent paper.

All our gas coma simulations are steady state solutions for one solar illumination condition at a time. Our simulated coma is therefore not time-dependent. This is a reasonable simplification considering that the

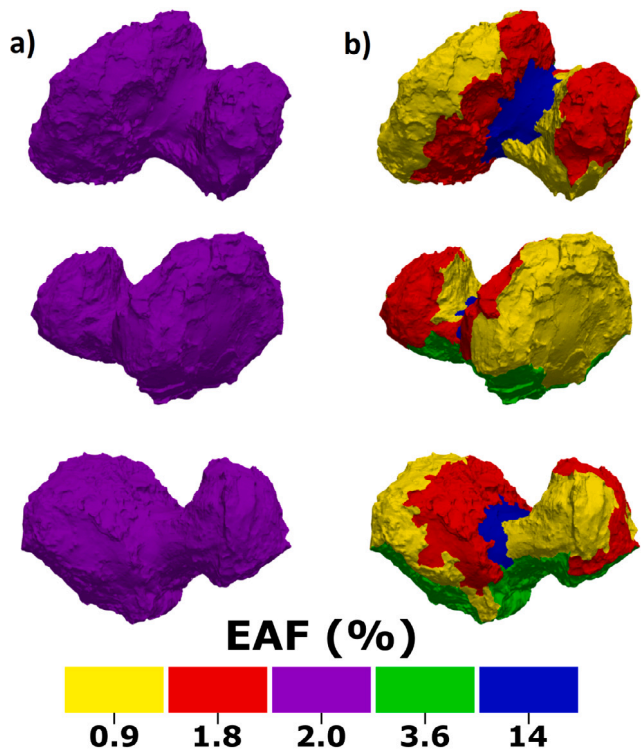

Fig. 3. Effective active fraction (EAF) maps for the simulations of the OSIRIS time series on the 11th April 2015. The model on the left (a) has a globally homogeneous EAF map. The model on the right (b) has regionally different EAF values. The regional EAF distribution is the same as was found for Spring Equinox (May 2015) in Marschall et al. (2019), but scaled down to match the total production rates in April 2015.

gas molecules are typically accelerated to speeds of >100 m/s in only a few seconds. This means they leave our simulation domain in the order of a few tens of seconds, which is quasi-instantaneous compared to the comet pre-perihelion rotation period of 12.4 h (Jorda et al., 2016).

DSMC example result. As an example of our gas simulation we show the result for the illumination conditions on the nucleus corresponding to image A. The slice through the simulation domain shows a plane normal to the line of sight from the spacecraft to the nucleus (Fig. 4). In the figure, we show the logarithm of the simulated H_2O number density. The model is based on the regionally inhomogeneous EAF map (Fig. 3b). Here, the non-illuminated nightside is inactive (the temperature of non-illuminated facets is set to 100 K). The direction of the sun in the image is marked with a white line. We can see that most of the activity is directed towards the sun as we expect for insolation-driven activity. The gas is also laterally expanding from the active dayside towards the nightside, but the gas densities on the nightside are typically ≥ 2 orders of magnitude below the number density observed on the dayside.

3.1.2. DRAG3D

DRAG3D is the name of our simulation code developed to study the dust dynamics in the first ten kilometres above the comet nucleus. It is an advanced version of the dust dynamics codes used in previous publications (see Gerig et al., 2018; Marschall et al., 2019, 2016, 2017), that now includes the shadowing of the dust coma by the comet nucleus. Similar model approaches have been published by, for example, Crifo et al. (2005), Combi et al. (2004, 2012) and Tenishev et al. (2011).

DRAG3D simulation pipeline. We simulate the dust field around 67P by propagating test particles through the DSMC gas field. The test particles are assumed spherical and we simulate the dynamical behaviour of 40 discrete size bins separately. Our test particles cover a radii range of ≈ 8 nm–0.3 mm corresponding to size parameters of $0.08 < x < 3265$ ($x = 2\pi r_d/\lambda_c$, with $\lambda_c = 612.6$ nm being the central wavelength for WAC filter 18). They have a density of 440 kg/m^3, a value which is a bit lower than the nucleus bulk density (Preusker et al., 2017; Pätzold et al., 2018). The applied equation of motion for the dust at any location inside the simulation grid (we use the same simulation grid as for the DSMC gas simulation) includes the drag force $\vec{F}_D$ from the gas flow and the opposing gravity force $\vec{F}_G$ from the nucleus acting on a particle of mass m_d and radius r_d at location $\vec{x}_d$:

$$m_d\vec{a}_d = \vec{F}_G + \vec{F}_D = m_d\vec{g}_{x_d} + \frac{1}{2}C_D m_g n_g \sigma_d |\vec{v}_g - \vec{v}_d|(\vec{v}_g - \vec{v}_d), \tag{7}$$

with $\vec{a}_d = \frac{d^2\vec{x}_d}{dt^2}$ the acceleration of the dust particle and $\vec{g}_{x_d}$ the local gravitational acceleration. The gravity field is calculated for the complex nucleus (see section 3.3.2 in Marschall et al., 2016) with constant bulk density of 537.8 kg/m^3 (Preusker et al., 2017; Pätzold et al., 2018). The drag force is dependent on the mass of the simulated gas molecules m_g (here H_2O), the local gas density n_g from the DSMC result, the geometric dust particle cross-section $\sigma_d = r_d^2\pi$, the difference in local gas and dust velocity $(\vec{v}_g - \vec{v}_d)$ and the drag coefficient C_D. C_D is calculated as (Crifo et al., 2005):

$$C_D = \frac{2\zeta^2+1}{\sqrt{\pi}\zeta^3}e^{-\zeta^2} + \frac{4\zeta^4+4\zeta^2-1}{2\zeta^4}erf(\zeta) + \frac{2(1-\epsilon)\sqrt{\pi}}{3\zeta}\sqrt{\frac{T_d}{T_g}}. \tag{8}$$

In these calculations the dust temperature T_d is set to be equal to the gas temperature T_g, the fraction of specular reflection $\epsilon = 0$ and

$$\zeta = \frac{|\vec{v}_g - \vec{v}_d|}{\sqrt{\frac{2kT_g}{m_g}}}, \tag{9}$$

with k being the Boltzmann constant. A fourth-order Runge–Kutta method with adaptive timestep is used to solve the equation of motion and the particles are tracked either until they reach the 10 km outlet boundary of the simulation domain or until they are redeposited on the surface of the nucleus. The acceleration due to gravity is the same

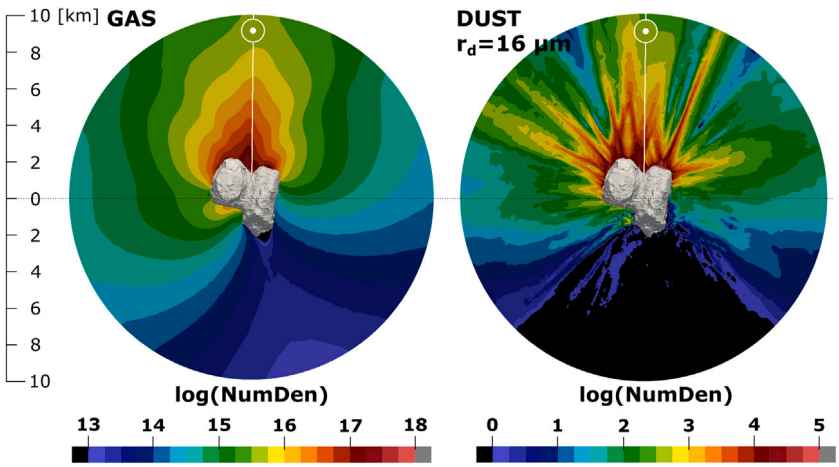

Fig. 4. Left: A slice through the gas number density result of a simulation with the inhomogeneous EAF map for the illumination conditions of image A. Right: Corresponding slice through the dust number density result of the dust flow field for particles of radius r_d = 16 µm. The Sun illuminates the nucleus at a latitude of ≈10° north and a longitude of 46° east in the Cheops coordinate frame. The direction to the Sun in the image is marked by a white line. The normal to the plane of the slice is pointing towards the spacecraft position.

for all particles independent of mass or size, but the drag acceleration for spherical particles of constant density is proportional to $1/r_d$ and thus gets smaller for larger particles. This means that gravity force has more influence on the particle trajectories of large particles, an effect which can be seen in the results for the larger dust size bins in the form of returning trajectories. To obtain the dust coma properties in the grid cells, such as dust number density or dust velocity, test particles are numerically weighted such that they reflect the actual number of particles leaving a surface facet. This number is determined by assuming a dust-to-gas mass production rate ratio Q_d/Q_g and scaling the dust flux to the gas flux accordingly. We set Q_d/Q_g to be constant over the whole surface of the comet. Dust properties per cell, such as number density and velocity, are then calculated by averaging over the corresponding dust property of all the test particles that crossed the cell at any point during the simulation taking into account the time the particle spent in that cell.

To produce artificial images that can be directly compared with OSIRIS images, the dust number density is integrated along lines of sight from the camera towards the nucleus. Points beyond the grid outlet boundary at 10 km are extrapolated using a $1/r^2$ law. This is again done for every simulated size bin separately, resulting in 40 partial images that are in a last step combined to generate the final artificial image including all dust sizes. The calculated column density n_{col} result for each size bin is weighted according to a power law particle size distribution function of the form:

$$n_{col}(r_d) \sim r_d^{-q}. \tag{10}$$

The power law index, q, is a free parameter in our model and has been varied for this work in half-integer steps between $2.0 \leq q \leq 4.0$. Measurements from the Cometary Secondary Ion Mass Analyzer (COSIMA; Kissel et al., 2007) indicate a cumulative power law dust size distribution exponent of $q = 1.8 \pm 0.4$ before spring equinox in May 2015 which is increasing to $q = 2.8 \pm 0.9$ towards perihelion for particles in the 30–150 µm size range (Merouane et al., 2017). The controlled size distribution in the model corresponds to the initial size distribution of particles ejected from the surface and is changed locally in the coma by the forces acting. The brightness in unitless reflectance values, R, for every partial image assuming an optically thin coma is calculated as:

$$R = n_{col}\sigma_{geo}Q_{scat}\frac{p(\phi)}{4\pi}. \tag{11}$$

$\sigma_{geo} = \pi r_d^2$ is the geometric particle cross section. The scattering properties, such as the scattering efficiency Q_{scat} and the phase function $p(\phi)$ as a function of the phase angle ϕ, are calculated using Mie theory and the algorithm of Bohren and Huffman (1983). A new addition to the DRAG3D code is now taking into account the shadow that is cast by the nucleus onto the nightside coma. In the image composition, grid cells shadowed by the nucleus get a reflectance of zero assigned and the shadowed grid cells are thus not contributing to the calculated brightness. As a final step, the partial images are combined to produce the total artificial image corresponding to a dust size distribution with a specific power law exponent q and dust-to-gas ratio Q_d/Q_g.

DRAG3D example result. As an example for a dust simulation result we show a slice through the dust flow field simulation of particles with radius r_d = 16 µm (Fig. 4, right). The DSMC gas field shown in the same figure served as an input to the DRAG3D pipeline for calculations of the local drag force that the gas is exerting on the dust. The shown dust result is merely one of the 40 dust fields simulated for particles with radii in the range between 8 nm–0.3 mm. The simulated dust coma is much more structured than the corresponding gas coma. The coma pattern visible in the simulation result mostly reflects the surface morphology and is not greatly influenced by the surface source distribution. This can be seen in Fig. 7 (a) showing a brightness profile around the azimuthal angle at 3 km distance from the nucleus centre of the inhomogeneous (blue) and the homogeneous (red) simulation results.

It has to be kept in mind that the slice through the dust field result cannot be directly compared to the corresponding OSIRIS image because, firstly, it is not a column integration through the whole coma and, secondly, it is just the result of one single dust particle size. An example of a final artificial image of the DRAG3D simulation is shown in Fig. 5 (a).

3.2. Simplified Keplerian model for large, gravity dominated particles

To test the influence of large particles on the coma brightness, we simulate a background of gravity dominated particles in a physically simplified model environment. We do this by tracing particles along Keplerian trajectories from a rotating spherical nucleus with a surface radius of 2 km. The sphere rotates with a rotation period of 12.4 h. The model takes into account the direction of insolation and the direction to the observer. In the model, particles are generated randomly on the sunlit hemisphere of the spherical nucleus. A particle is released from the surface without assuming any release mechanism and it obtains a randomised initial speed. The initial speeds follow a half-Gaussian velocity distribution function (VDF) inhibiting negative velocities towards

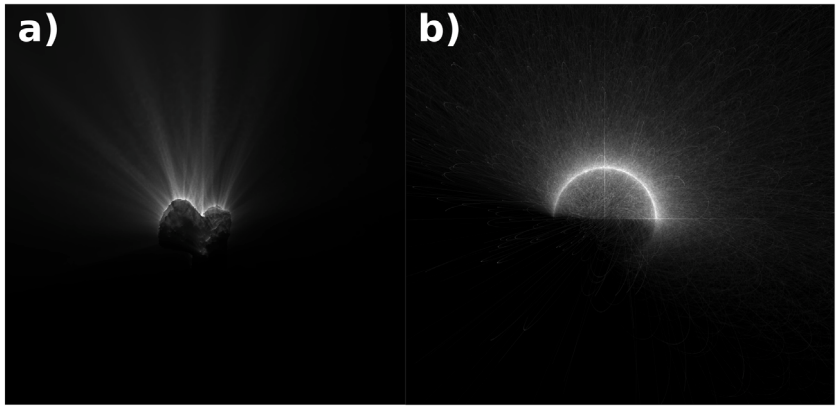

Fig. 5. (a) Artificial image generated with the DRAG3D code corresponding to OSIRIS image A with a homogeneous EAF and without nightside activity. We show the image corresponding to dust size distribution power law exponent q = 3.0 and Q_d/Q_g = 1. It is zoomed in and enhanced in brightness. (b) Zoomed in and stretched artificial simulation image of a background of large gravitationally dominated particles. This is the result corresponding to the input parameters of model II in Table 2.

the nucleus surface. The mean speed determining the width of the VDF is a free parameter of the model. A randomised lateral deviation to the main velocity direction, which is defined perpendicular to the surface, is added and is another free parameter. The initial velocity of the released particle also includes a tangential velocity component arising from nucleus rotation. Because the gravity dominated particles move by definition at low speeds comparable to or below the escape velocity of 67P, these particles stay close to the nucleus on time scales that are comparable to its rotation period. Therefore, the effect of nucleus rotation on the trajectories cannot be neglected. The model accepts two modes of source strength distributions over the sunlit hemisphere. Either the source strength is homogeneous over the whole illuminated hemisphere or the source strength is weighted with the cosine of the incidence angle. The latter option emulates insolation driven activity with the maximum source strength at the sub-solar point. The particle is finally tracked along its trajectory in finite time steps over 5.4 comet rotations (66.67 h or $60 \cdot 10^3$ time steps of 4 s). The particle trajectory is governed by gravitational acceleration and an optional constant acceleration in a specific direction. With the latter option, acceleration such as that arising from solar radiation pressure can be tested in the model. After particle tracking, the particle positions are integrated along lines of sight into a 2D image grid. The image dimensions are fixed to 2000 x 2000 and the absolute grid spacing, which corresponds to the pixel spatial resolution, is determined by the pixel resolution of the OSIRIS image which the background is compared to. From the integrated particle number density per image grid space, a filling factor is calculated by multiplication with the particle cross section. For the calculation of the final image brightness, we assume that the simulated large particles scatter sunlight as if they were chunks of the surface of 67P. This is a reasonable assumption, since millimetre to decimetre sized particles have spatial dimensions that are very large compared to the visible wavelengths at which the images are acquired. Therefore, we use the Hapke phase curve (Hapke, 1981, 1993, 2002) which was determined for the surface of 67P by Fornasier et al. (2015). We note that the particle radius and thus the particle masses do not influence the dynamical result because the trajectories are governed by gravity alone. The particle radius only plays a role in determining the final brightness of the image, where it enters in the form of a filling factor. This means that we can calculate the final image brightness for any particle size (dust radius r'_d) by multiplying the result for the particle with radius r_d with a factor of $(r'_d/r_d)^2$. As an example, we show in Fig. 5 (b) the resulting artificial image of a background simulation of large gravitationally bound particles. It was generated with the input parameters of model II in Table 2.

4. Results

The results section of this paper contains three subsections:

- 4.1 DS:NS ratio in dust dynamics simulations
- 4.2 DS:NS ratio in a gravity dominated large particle background
- 4.3 Time dependence of DS:NS inbound to perihelion

In the first Section 4.1, we present and discuss the results of our coma dust dynamics model corresponding to the four OSIRIS images from Section 2. We compare DS:NS ratios and dust outflow behaviour of two coma models with different source distributions on the surface with a coma model that additionally includes nightside activity. We discuss the potential of added nightside activity to explain the observed DS:NS ratios and dust outflow behaviour in OSIRIS images.

In the second Section 4.2, we present and discuss the results from a simplified Keplerian simulation of large gravitationally bound coma particles. We explore a large parameter space and compare DS:NS ratios of different model input conditions with each other and with the OSIRIS observations. We discuss the potential of large gravity dominated particles in the inner coma to explain the observed DS:NS ratios and dust outflow behaviour in OSIRIS images.

In the third Section 4.3, we show the temporal evolution of DS:NS ratios in OSIRIS images as a function of days to perihelion and discuss our previous results in the context of the mission timeline to perihelion.

4.1. DS:NS ratio in dust dynamics simulations

In a series of full dynamics simulations with the DSMC and DRAG3D pipeline, we simulated the gas and dust coma corresponding to the four OSIRIS observations in the subset chosen for analysis (Table 1). We ran simulations for each of the four observational geometries with a globally homogeneous EAF and with a regionally inhomogeneous EAF map (Fig. 3 a and b). We compare the DS:NS ratios calculated from the artificial simulation images (image analysis according to Section 2.3) with those of the corresponding OSIRIS images. All DS:NS ratios are shown in Fig. 6. The star and square symbols indicate the results for the inhomogeneous and the purely insolation driven model, respectively. The different colours from light pink to dark red (left to right in a symbol group) mark results for different size distributions. The power law size distribution function (Eq. (10)) in our dust simulations is determined by q. It is immediately clear from the graphic, that the DS:NS ratios for all the DRAG3D simulations without nightside activity are very high: All of them are above 10, which is, even in the best case, more than a factor 4 higher than the ratios observed in the OSIRIS images. This implies that in our simulations we see far fewer particles on the nightside relative to the dayside than is observed by OSIRIS at

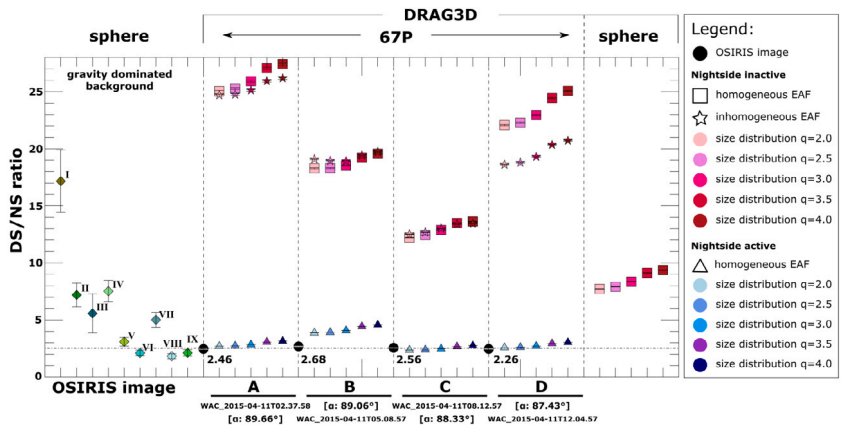

Fig. 6. Overview of the results of DS:NS ratios from OSIRIS images and corresponding simulations. The black dots represent the OSIRIS DS:NS results from image analysis. The square and star symbols represent results of the full dust dynamics simulations with the DRAG3D code with a homogeneous EAF and a inhomogeneous EAF, respectively. The triangle symbols represent results of the DRAG3D simulations with an artificially added nightside H_2O activity. On the right of the graphic, results of a simulation with a spherical nucleus is shown to test the influence of the complex nucleus shape on the DS:NS ratios. On the left we show DS:NS ratios of simulations with the simplified Keplerian model for a gravitation dominated large particle background (diamonds). The numbers besides the diamond symbols correspond to the numbers of the model initial conditions in Table 2. The errors of DS:NS are indicated with errorbars. For the OSIRIS analysis and the results from the dynamics simulations the errors are very small (in the order of 1%) and the errorbars are therefore mostly contained in the respective symbols. The results are discussed in more detail in Sections 4.1 and 4.2. (For interpretation of the references to colour in this figure legend, the reader is referred to the web version of this article.)

67P. A particle size distribution with $q = 2.0$ as a rule leads to lower DS:NS ratios. This is expected, because the larger simulation particles, which dominate the size distribution for smaller power law exponents, are more likely to fall back onto the nucleus rather than reach escape velocity and thus may be transported on ballistic trajectories towards the nightside of the nucleus. Last but not least, we note that the source distribution on the surface does not have a large influence on the result, although the inhomogeneous EAF map seems to lead to slightly better results for image D.

In Fig. 6, the simulation cases with 10% of the activity from the nightside are shown as blue triangles. The colour from light to dark blue (left to right in a symbol group) indicate results with different size distribution power law indexes from 2.0–4.0 varied in half-integer steps. The DS:NS brightness ratios in the simulation cases with added nightside activity are in the value range between 2.4–4.6, which is close to the values observed in OSIRIS images.

This is even better illustrated when looking at a plot showing the polar distribution of brightness around the nucleus. In Fig. 7, we show a brightness profile at 3 km distance from the nucleus centre. The black profile is the brightness distribution in our OSIRIS example image A. Most of the dust activity is pointed roughly in the sunward direction (270°) as is expected for insolation driven dayside activity. This is in good agreement with Tubiana et al. (2019), who report for OSIRIS and VIRTIS-M observations from 27. April 2015 that the main dust activity peaks at 0° subsolar longitude (sunward direction) and that water is the main driver for dust activity coming from the sunlit dayside of the comet. The red and blue lines show the polar profile at 3 km nucleocentric distance in the simulation image with a homogeneous and an inhomogeneous EAF, respectively, and no nightside activity. The orange line shows the corresponding polar profile for a simulation case with a homogeneous EAF and 10% activity from the nightside. It fits the OSIRIS profile much more closely than the red and blue profiles of the models without nightside activity. It especially reaches the brightness level of the observations over the nightside (angle range 0–180°). On the dayside (angle range 180–360°), all three models reproduce the general outflow pattern well, showing that the dayside activity is modelled well by an insolation driven H_2O coma. We want to stress at this point, that it was not the intention of this work to try to fit the source distribution on the nucleus surface to match outflow pattern exactly. The brightness peak at 350° is almost certainly arising from an inhomogeneity in surface source distribution that is not included in our EAF maps.

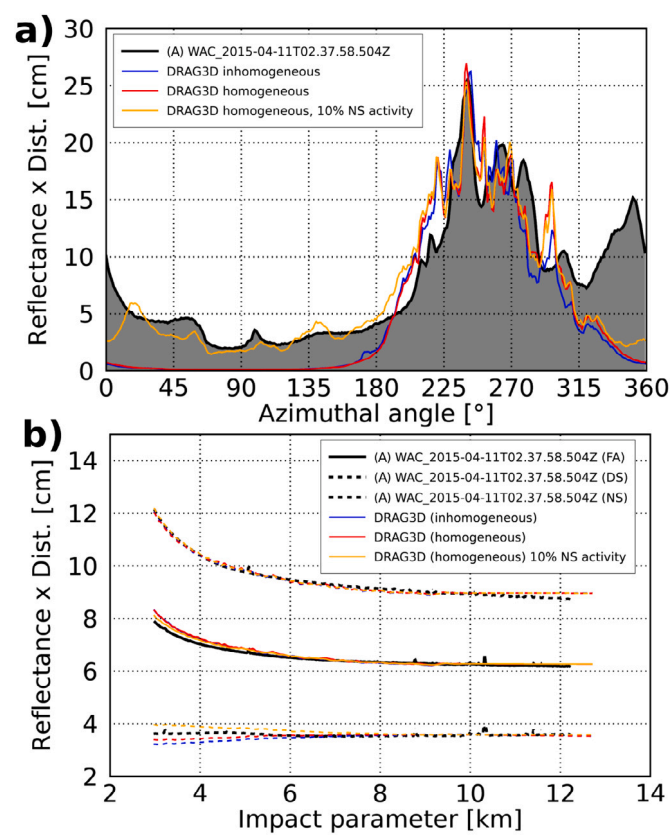

Fig. 7. (a) Brightness distribution with polar angle around the nucleus in OSIRIS and corresponding artificial simulation images. Nightside activity (orange line) is needed to fit the brightness level observed on the nightside of 67P. (b) Azimuthal average profiles in the same OSIRIS and simulation images to test the general outflow behaviour in the simulation models.. (For interpretation of the references to colour in this figure legend, the reader is referred to the web version of this article.)

The outflow behaviour of all three models fit the general outflow behaviour observed at 67P well. Especially on the dayside only little deviations from the azimuthal average profile of the OSIRIS image is observed. This means that we fit the dayside activity extremely well

with our dust dynamics model. The azimuthal average profile is not very sensitive to source distribution on the surface because it is averaged over the whole polar angle range and therefore all three models give nearly the same result for the dayside profile and the dayside dominated full angle profile. However, when looking at the nightside profiles the differences between the models are more significant. The added nightside activity modifies the profile in the right direction for a better fit with the OSIRIS profiles, but over-corrects the profile indicating that 10% of the total activity coming from the nightside is probably a slight overestimation.

Because we only simulate particles with a maximum particle radius of 0.32 mm, an additional fraction of even larger particles dominated by gravity and transported towards the nightside on bound or ballistic trajectories could also potentially lead to enhanced brightness in the nightside coma and thus to smaller DS:NS ratios. We explore and exclude this possibility of brightness contributions to the nightside by larger particles (mm-cm-dm size) dominating the observed coma in Section 4.2, where we present the results of simulations of a background of gravity dominated large particles.

DS:NS ratio for a spherical nucleus. To study the influence of the complex shape of 67P we can compare two simulations with the same initial conditions but one using the complex nucleus and one using a spherical nucleus as the inlet surface. Complementary to the simulation with the homogeneous EAF, we simulate insolation-driven outgassing from a homogeneous sphere without nightside activity. From the final results of our simulation we calculated the DS:NS brightness ratio for the sphere and show them in Fig. 6 on the far right of the graphic. The calculated DS:NS ratios in the spherical case have values between 7.7–9.3, which is compared to the OSIRIS observations still more than a factor 3 too high, but lower than the ratios we observe in the dynamics simulations with the complex nucleus with an inactive nightside. Therefore, it seems that the assumption of a spherical nucleus leads to underestimating the DS:NS. This is important to keep in mind for the next section, where we study a spherical nucleus in a simplified modelling approach.

4.2. DS:NS ratio in a gravity dominated large particle background

Because we only simulate particles with a maximum particle radius of 0.32 mm in our DRAG3D simulation, an additional fraction of even larger particles dominated by gravity and transported towards the nightside on bound or ballistic trajectories could potentially lead to enhanced brightness in the nightside coma and thus to smaller DS:NS ratios. Larger dust particles of millimetre, centimetre or even up to decimetre size are not efficiently accelerated to escape velocity via gas drag and are therefore more likely to fall back onto the nucleus after an initial ejection from the surface. This means that they are moving at low speeds along ballistic trajectories or even in gravitationally bound orbits around the nucleus, where they have a chance to appear on the nightside and contribute to the brightness there. To test the magnitude of this effect, we simulate a background of large gravity dominated particles with the model described in Section 3.2. We tested nine different model set-ups and the initial parameter conditions for every tested model are listed in Table 2. The results in DS:NS are shown as green diamonds on the left side in Fig. 6. The numbers besides the diamond symbols correspond to the numbers of the model initial conditions in Table 2. The errors in DS:NS are higher than for the OSIRIS analysis or the dynamics simulations because, firstly, the model uses lower statistics and, secondly and more importantly, the flow behaviour does not tend towards force-free radial outflow in the case of gravity dominated particles and we therefore have a gradient in the profile at the location where we calculate the DS:NS ratio.

4.2.1. Models I and II: The effect of insolation-driven outgassing on DS:NS

The only difference in the initial conditions between models I and II is, that in model I, the simulated particles over the sunlit hemisphere are weighted with a cosine distribution to simulate insolation-driven activity, whereas in model II the particles are homogeneously distributed over the whole hemisphere. This change of the source distribution in the input conditions has a significant effect on the resulting DS:NS ratio, which is for model II with the homogeneous distribution about 2.4 times lower than for model I (see Fig. 6). This effect can be explained with the fact that the regions close to the day-night-side terminator release more particles in the homogeneous case (model II) than in the case where the amount of particles released is weighted with the cosine of the incidence angle (model I). The initial speeds of particles released close to the terminator have an average angle of 90° with the sun incidence direction and because of the randomisation of the initial speed direction, about half of the particles already start off with velocities towards the nightside and hence immediately appear above the nightside and the DS:NS ratio is therefore lower in model II. The same effect of the homogeneous versus the cosine distribution can be seen when comparing the results of models V and VI.

4.2.2. Models III and IV: The effect of the initial mean speed on DS:NS

When comparing model II with models III and IV, we can see that the mean speed we give to the initial velocity distribution of the particles does not have a large influence on the final result. The trend in the modelled data shows that we can expect slightly smaller DS:NS ratios the slower the particles move on average, but the relatively small differences between the ratios (compare Fig. 6) suggests that the mean speed is not the most decisive parameter for DS:NS in the simulation. We note that, even for a very low mean speed of 0.3 m/s, the DS:NS ratio in the result is, with a value of 5.58, still too high compared to the OSIRIS observations.

4.2.3. Models V–VIII: The effect of an anti-sunward acceleration on DS:NS

From a comparison of results of models I and V or model II and VI, it is clear that an additional force in the model realised through an additional acceleration term in the applied equation of motion can reduce the DS:NS ratios (see Fig. 6). In models V and VI, an additional acceleration of $3.0 \cdot 10^{-6}$ m/s^2 in an anti-sunward direction has been introduced in the model. As mentioned before, this could simulate, for example, a force such as solar radiation pressure. We note here, that outgassing of coma dust particles heated by the Sun could potentially also produce a force in an anti-sunward direction through directed rocket force. In models V and VI, the magnitude of the additional acceleration was chosen such that we obtain about the values for DS:NS that we expected from the OSIRIS observation. When calculating more realistic values for the radiation pressure acceleration on a particle of 0.01 m radius at 1.89 AU (April 2015), we arrive at acceleration values that are almost an order of magnitude lower than that used in models V and VI. We calculate a rough first order estimate for the acceleration of a particle with radius r_d caused by radiation pressure as

$$a_{rad} = \frac{3L_\odot}{8\pi D_\odot^2 c r_d \rho}, \tag{12}$$

with $L_\odot$ the total average solar luminosity, $D_\odot$ the heliocentric distance, c the speed of light and ρ the particle density. This equation is based on the assumption that the particle is a perfect reflector and back-scatterer (Burns et al., 1979). This is most certainly not the case for real cometary dust particles (the nucleus has a geometric albedo of 6.5% Fornasier et al., 2015 and the scattering phase curves suggest a significant amount of forward scattering Bertini et al., 2017) and the calculated accelerations are therefore strict upper boundaries. A perfectly absorbing particle would experience a factor of 2 smaller acceleration caused by radiation pressure. In addition, we neglect solar gravity, which would further decrease the anti-sunward acceleration. In models VII and VIII, we tested upper boundary values of solar

Table 2
List of the input parameters, such as the mean speed v_m, the random speed v_r, the additional acceleration a_+ and the particle radius r_d, tested in the model to simulate the background of gravity dominated large particles. COS = YES indicates that a cosine distribution over the illuminated hemisphere was used. The particle density was in all runs set to 500 kg/m^3. Each diamond on the left in Fig. 6 shows the DS:NS ratio result of one of the large simulations. The numbers in the figure correspond to the model numbers in this table. The models that produce DS:NS ratios close to the observations are highlighted in grey.

No.	v_m [m/s]	v_r [m/s]	$a_+[m/s^2]$	r_d [m]	COS	DS:NS
I	0.6	0.01	0	0.01	YES	17.16 ± 2.74
II	0.6	0.01	0	0.01	NO	7.19 ± 1.05
III	0.3	0.01	0	0.01	NO	5.58 ± 1.72
IV	1.0	0.01	0	0.01	NO	7.52 ± 0.95
V	0.6	0.01	-3.0E-6	0.01	YES	3.09 ± 0.37
VI	0.6	0.01	-3.0E-6	0.01	NO	2.10 ± 0.26
VII	0.6	0.01	-3.86E-7	0.01	NO	5.01 ± 0.65
VIII	0.6	0.01	-3.86E-6	0.001	NO	1.82 ± 0.22
IX	0.6	0.5	0	0.01	YES	2.11 ± 0.29

radiation acceleration for particles of two different radii. Although it was mentioned before that the gravitationally dominated trajectories are the same for all particle sizes, the magnitude of the acceleration caused by radiation pressure depends on particle size. In model VII the particle with a radius of 0.01 m has an additional acceleration of $3.86 \cdot 10^{-7}$ m/s^2. In model VIII the particle with radius 0.001 m feels a 10 times larger additional acceleration of $3.86 \cdot 10^{-6}$ m/s^2. This has a very noticeable effect on the result of the DS:NS ratio: The DS:NS ratio for the smaller particles, which feels a stronger additional acceleration, is about a factor of 2.75 smaller than the ratio for particles with a 10 times larger radius and lies with 1.82 ± 0.22 just a bit below the range of the DS:NS ratios of the OSIRIS images. On the other hand, smaller particles are affected more strongly by the gas drag and this would add an acceleration mostly radially outward from the surface which is not included in our simplified model here. But as we can see from our full dynamics model this leads to much higher DS:NS ratios that are not compatible with the observation. So including radiation pressure or similar anti-sunward acceleration does not help to explain the observed DS:NS ratio.

4.2.4. Model IX: The effect of lateral deviation from the initial speed direction perpendicular to the surface on DS:NS

In model IX the magnitude of the random speed, which is controlling the lateral deviation from the initial speed direction perpendicular to the surface, has been increased by a factor of 50. The rest of the parameters were kept the same as in model II. In this test case IX, we reach a DS:NS ratio as low as in the observations (compare Fig. 6). It is not surprising, that an increased lateral deviation from the direction perpendicular to the surface increases the particle transport towards the nightside and thus leads to low DS:NS ratios. However, the model case we show here is extreme, with the mean of the lateral component (v_r = 0.5 m/s) of the initial velocity being more than 83% of the mean speed component perpendicular to the surface (v_m = 0.6 m/s). This effectively results in a wide distribution of ejection angles. In our full dynamics simulations with the DRAG3D pipeline, we do not model any mechanism of ejection for dust particles. This means that the particles are lifted off the surface by gas drag and the particle velocities are dominated by the gas velocity immediately above the surface, which is strongly aligned with the local surface normals. The angular distribution of gas and dust velocity in DSMC and DRAG3D simulation results right above the surface measured to the local surface normals has a much narrower distribution. This result, especially the result of our gas dynamics simulation, indicates that large amount of lateral transport driven by gas drag (i.e. surface "breezes" as was suggested as a mechanism to enhance DS:NS ratio at 1P/Halley by Keller and Thomas (1989)) is not to be expected at 67P under the assumption of smooth homogeneous outgassing on the dayside. Nevertheless, a particle ejection mechanism for dust particles leading to large deviations of ejection directions from the local surface normal could contribute to enhance lateral particle transport towards the nightside and thus decrease the DS:NS brightness ratio.

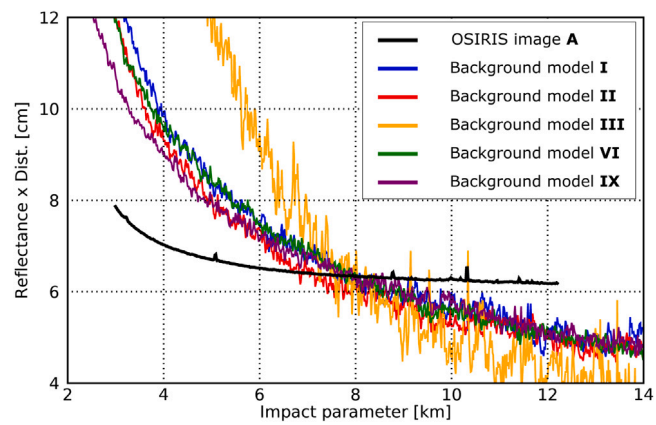

Fig. 8. Full angle azimuthal average profiles of the OSIRIS image A (black line) in comparison with the azimuthal average profiles of some of the gravity driven background simulations. See Table 2 for the corresponding model parameters. The figure shows that a coma in which gravity dominated particles constitute the major part of scattering centres does not match the observed outflow behaviour at 67P. The profiles are normalised to fit the OSIRIS observation at 8 km.

4.2.5. The azimuthal average in the gravity dominated background

We have shown that gravity dominated models require some extreme conditions to match the low DS:NS of the observations. But we have not yet used all the observational information. When looking at the azimuthal average profiles from the gravity dominated background models, it immediately becomes clear that they are very different from the OSIRIS profile. In Fig. 8 the azimuthal average profiles of a few selected large particle background models (see Table 2) are shown in comparison with the azimuthal average profile of OSIRIS image A. While the OSIRIS profile shows a decrease close to the nucleus and tends towards free radial outflow with increasing impact parameter (*1/r* behaviour i.e. a flat curve in the plot), all model profiles also show a steep decrease close to the nucleus but do not converge towards a *1/r* behaviour. This makes it clear, that we are not observing a dust coma dominated by large particles. If such particles were present, their outflow behaviour has to be masked by the outflow behaviour of particles whose movement is initially governed by gas drag followed

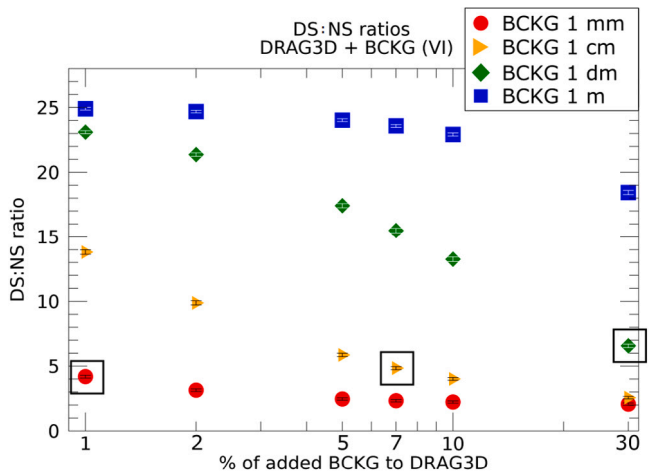

Fig. 9. DS:NS ratios of a DRAG3D simulation result (inhomogeneous for OSIRIS image A) as a function of mass percent added in the form of a large particle background (BCKG in the figure). The background was separately calculated and added for four different particle sizes (1 mm, 1 cm, 1 dm, 1 m). Data points for which azimuthal average profiles are shown in Fig. 10 are shown in black frames.

by decoupling from the flow. To test how many large particles can be masked in a drag dominated coma, which is needed to fit the OSIRIS observations, we added a background of large particles simulated with the Keplerian model in different percentages of mass production rate to our DRAG3D simulation results. At the same time the DS:NS ratios in these added model results were determined and are shown in Fig. 9. The large particle background of model VI was chosen as an example and added in different percentages of total mass production rate to the result of the DRAG3D simulation with the inhomogeneous EAF corresponding to OSIRIS image A. The different symbols indicate different particle sizes in the modelled background. The figure shows that for particles of $r_d \geq 1$ cm more than 30% of the mass has to be concentrated in the large particle background to obtain DS:NS ratios close to the observed values. In the case of a background of mm-sized particles lower mass fractions are needed to achieve low DS:NS ratios. However, particles in the mm-size range are, for the level of production rate we are considering here, probably not dominated by gravity but still governed by gas drag (Fig. 49 in Marschall, 2017 for spherical simulations) and are thus more likely to show outflow behaviour and DS:NS like we observe in our DRAG3D simulations.

When looking at the azimuthal average profiles of the models with the added large particle background in Fig. 10, we can see that it is not possible to mask enough gravity dominated particles to explain DS:NS ratios as low as in the OSIRIS observations. We show three model curves (red, orange and green) that correspond to the indicated models and data points in Fig. 9. In both, the azimuthal average profiles over the dayside (a) and over the nightside (b), the model profiles with added large particle background show outflow behaviours that are dominated by the gravity dominated background and are thus not fitting the profile from the OSIRIS observation (black line). At the same time, the DS:NS ratio in all three model cases is still too high to match the OSIRIS observations, as is clear from Fig. 9, and an even higher mass fraction of large particles would be needed to further enhance the background outflow. Especially from comparing the nightside azimuthal profiles it is apparent that the gravity dominated background does not fit the dust outflow behaviour at 67P. The OSIRIS observation shows an almost constant profile but the gravity dominated background decreases almost linearly with increasing impact parameter. However, the full dynamics simulation (blue line) and, as mentioned before, the full dynamics simulation with 10% activity added on the nightside (pink line) both show a nightside outflow behaviour that is matching

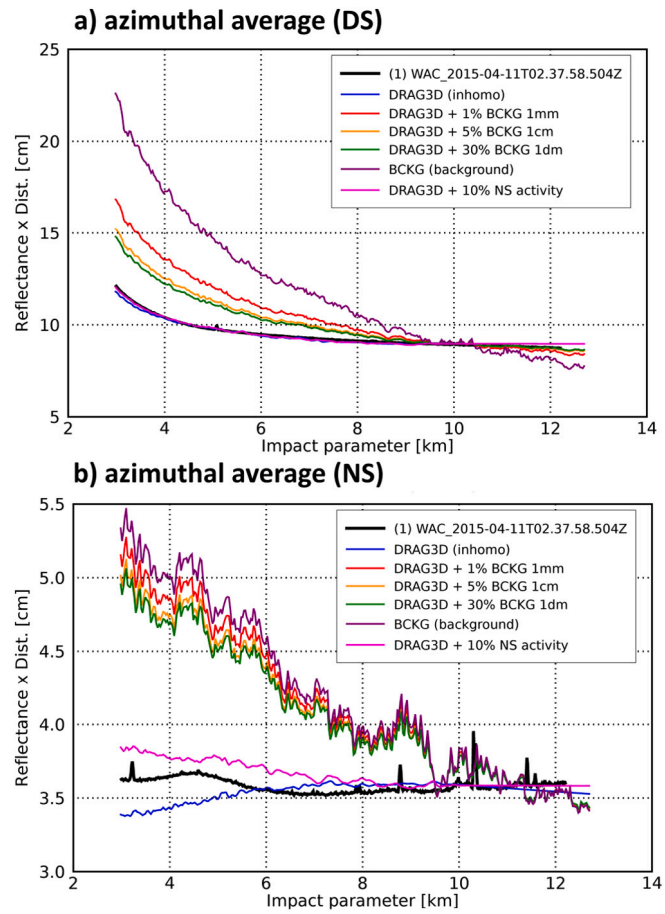

Fig. 10. Dayside and nightside azimuthal average profiles of the OSIRIS image A (black line) in comparison with the azimuthal average profiles of different simulation models. In three of the models a percentage of 1%, 5% and 30% of mass was added to the final simulation result in the form of a gravity dominated background (BCKG) of three different particle sizes (1 mm, 1 cm, 1 dm). All profiles are normalised at 10 km. When comparing dayside and nightside profiles, note the different scales of the y-axis. (For interpretation of the references to colour in this figure legend, the reader is referred to the web version of this article.)

the observations much better. Therefore, a background of large gravity dominated particles appearing on bound or ballistic orbits above the nightside cannot explain the DS:NS brightness ratio and the dust outflow behaviour observed at 67P.

4.3. Time dependence of DS:NS inbound to perihelion

Finally, we show the variation of DS:NS ratios as a function of days to perihelion. For this we enlarged our original image subset of OSIRIS images by adding all available full-frame images that show the diffuse dust coma out to at least 12 km from the nucleus and that are taken at a phase angle of 90 ± 3°. Additionally, we only consider images acquired with high exposure times equal to or above 7.6 s to ensure a sufficient signal-to-noise ratio in the coma. We excluded all images for which an error with the mechanical shutter (Keller et al., 2007) was recorded during acquisition. We apply the same image analysis approach as described in Section 2 and the resulting DS:NS ratios are shown as grey points in Fig. 11. The red diamonds in the same figure represent weekly mean values (averaged over data inside 7-day bins) to correct for daily variations in DS:NS. The associated error bars represent the statistical standard deviation over the spread out data points. We observe that the DS:NS brightness ratio stays on approximately the same level from February to mid-July 2015 and increases significantly in the last 30

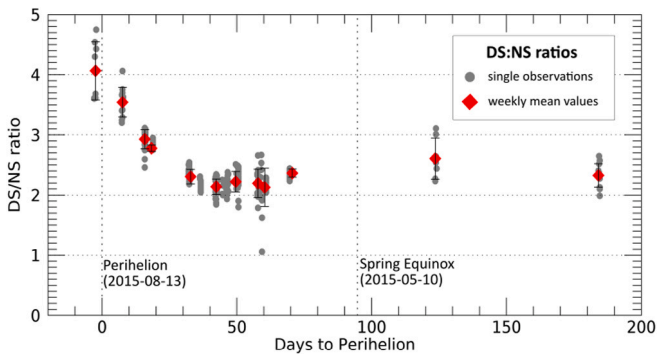

Fig. 11. DS:NS shown as a function of days to perihelion. The grey points indicate single data points from OSIRIS images inbound to perihelion and the red diamonds show weekly mean values with the corresponding statistical errors. Only OSIRIS images with a phase angle in the range 90 ± 3° and WAC Filter 18 were considered.

days towards perihelion. However, the dataset is fragmentary due to the specific selection criteria necessary for this analysis and the trend can thus not be observed continuously. The highest value in our dataset occurs 2.4 days after perihelion and the mean DS:NS value reaches 4.07 ± 0.49. This suggests that the increase in dayside activity and therefore the increased brightness of the dayside coma does not result in the same increase in the observed nightside brightness. We suggest that this is an indication that H_2O outgassing from the dayside becomes increasingly dominant as the driver of dust activity as the comet approaches the Sun. We shall address this in a subsequent study.

We also note at this point the data point (≈ 60 days to perihelion) that seems very close to a DS:NS ratio of 1 which would indicate a nightside as bright as the dayside. The corresponding OSIRIS image (W20150614T185006518ID4FF18) seems to have captured a moment where a large dust event is directed into the nightside and adding brightness to the nominal nightside coma.

5. Summary and conclusion

We analysed and modelled a selected subset of four OSIRIS images acquired during one comet rotation on 11. April 2015. A low DS:NS coma brightness ratio of 2.49 ± 0.18 was determined as an average of all four analysed images. The outflow behaviour in the dayside coma analysed in the form of azimuthal average profiles shows a steep decrease close to the nucleus that converges towards force-free radial outflow (i.e. constant behaviour) beyond 10 km from the nucleus centre. The full angle profile is mostly dominated by the dayside outflow behaviour. The nightside outflow profile follows a $1/r$-behaviour.

We compared the results of the OSIRIS image analysis with results of our DRAG3D simulation pipeline. We tested three different models: One with a homogeneous EAF, the second with an inhomogeneous EAF scaled from Marschall's map for spring equinox in May 2015 (Marschall et al., 2019) to match the production rates in April 2015. The third tested model has a homogeneous EAF and 10% of the total mass production rate coming from non-illuminated areas on the nucleus (i.e. the nightside and shadowed areas on the dayside). Analysis shows that the first two models produce DS:NS coma brightness ratios that are factors of 4–10 too high, whereas the simulation model with added nightside activity at a level of 10% of the total production rate produces DS:NS ratios in the correct range compared with the OSIRIS observations. The azimuthal average profiles of all three tested DRAG3D models fit well to the corresponding OSIRIS profiles, showing that the general outflow behaviour in the full dynamics simulations matches the observations. The azimuthal average profile for the nightside is modified in the right direction to improve the fit to the OSIRIS data by the added nightside activity. However, we note that in detail 10% activity on the nightside might be a slight overestimation when looking at our test case.

Further, a background of gravity dominated large particles on ballistic or bound trajectories was tested and excluded as a possible explanation for low DS:NS ratios in the observations. A simplified model where particles were tracked on Keplerian orbits from a spherical nucleus was used in the tests. The results show that we can indeed reach such low DS:NS ratios in our simulations but only if the model is pushed to its limits, e.g., by including an additional anti-sunward acceleration, discarding insolation-driven activity or increasing the lateral velocity component significantly above the level expected from gas kinetics simulations. In addition, the simplified model uses a spherical nucleus which in itself leads to lower DS:NS ratios than simulations with the complex shape. Furthermore, the outflow behaviour of the simulated large particle background does not match OSIRIS observations of the azimuthal average with distance and not enough large gravity dominated particles can be masked by dayside activity dominated by gas drag to fit both the low DS:NS ratios and the azimuthal average profiles. Therefore, we conclude that some amount of direct activity from the nightside of the nucleus is needed to explain all aspects of the OSIRIS observations consistently. Nightside activity has been reported before in the form of single dust events described as jet-like features or dust plumes emanating from non-illuminated surfaces of the comet in the first few hours after local sunset (Shi et al., 2016; Rinaldi et al., 2019) or a few hours before local sunrise (Knollenberg et al., 2016). In our study, however, we considered continuous outgassing and dust emission from non-illuminated surfaces to explain the observed nightside activity. Such outgassing is probably driven by sublimation of a sub-surface super-volatile such as CO_2 or CO and not H_2O (Bockelée-Morvan et al., 2015). The DS:NS ratio is increasing with decreasing heliocentric distance and reaches a maximum value of about 4.07 ± 0.49 at 2.4 days after perihelion in our dataset. The increase in DS:NS approaching perihelion may be indicative of increasing H_2O domination as the comet approaches the Sun. Our future work will include the application of a more advanced thermal model and outgassing of CO_2 in addition to water in our coma simulation to study the effect and plausibility of super-volatile outgassing as the driver of nightside activity as described in this paper.

Declaration of competing interest

The authors declare that they have no known competing financial interests or personal relationships that could have appeared to influence the work reported in this paper.

Acknowledgements

The team from the University of Bern is supported through the Swiss National Science Foundation under the grant 200020_178847 and through the NCCR PlanetS, Switzerland.

Raphael Marschall acknowledges the support from the Swiss National Science Foundation grant 184482.

Calculations were performed on UBELIX (http://www.id.unibe.ch/hpc), the HPC cluster at the University of Bern.

OSIRIS was built by a consortium led by the Max-Planck- Institut für Sonnensystemforschung, Göttingen, Germany, in collaboration with CISAS, University of Padova, Italy, the Laboratoire d'Astrophysique de Marseille, France, the Instituto de Astrofísica de Andalucia, CSIC, Granada, Spain, the Scientific Support Office of the European Space Agency, Noordwijk, The Netherlands, the Instituto Nacional de Técnica Aeroespacial, Madrid, Spain, the Universidad Politéchnica de Madrid, Spain, the Department of Physics and Astronomy of Uppsala University, Sweden, and the Institut für Datentechnik und Kommunikationsnetze der Technischen Universität Braunschweig, Germany.

We want to thank H. Sierks, C. Tubiana and C. Güttler for their clarifications and support concerning the OSIRIS sigma map S/N ratio calculations.

References

Bertini, I., La Forgia, F., Tubiana, C., Güttler, C., Fulle, M., Moreno, F., Frattin, E., Kovacs, G., Pajola, M., Sierks, H., Barbieri, C., Lamy, P., Rodrigo, R., Koschny, D., Rickman, H., Keller, H.U., Agarwal, J., A'Hearn, M.F., Barucci, M.A., Bertaux, J.-L., Bodewits, D., Cremonese, G., Da Deppo, V., Davidsson, B., Debei, S., De Cecco, M., Drolshagen, E., Ferrari, S., Ferri, F., Fornasier, S., Gicquel, A., Groussin, O., Gutierrez, P.J., Hasselmann, P.H., Hviid, S.F., Ip, W.-H., Jorda, L., Knollenberg, J., Kramm, J.R., Kührt, E., Küppers, M., Lara, L.M., Lazzarin, M., Lin, Z.-Y., Moreno, J.J.L., Lucchetti, A., Marzari, F., Massironi, M., Mottola, S., Naletto, G., Oklay, N., Ott, T., Penasa, L., Thomas, N., Vincent, J.-B., 2017. The scattering phase function of comet 67P/Churyumov-Gerasimenko coma as seen from the Rosetta/OSIRIS instrument. Mon. Not. R. Astron. Soc. 469, S404–S415.

Bieler, A., Altwegg, K., Balsiger, H., Berthelier, J.-J., Calmonte, U., Combi, M., De Keyser, J., Fiethe, B., Fougere, N., Fuselier, S., Gasc, S., Gombosi, T., Hansen, K., Hässig, M., Huang, Z., Jäckel, A., Jia, X., Le Roy, L., Mall, U.A., Rème, H., Rubin, M., Tenishev, V., Tóth, G., Tzou, C.-Y., Wurz, P., 2015. Comparison of 3D kinetic and hydrodynamic models to ROSINA-COPS measurements of the neutral coma of 67P/Churyumov-Gerasimenko. Astron. Astrophys. 583, A7.

Bird, G.A., Brady, J.M., 1994. Molecular Gas Dynamics and the Direct Simulation of Gas Flows, Vol. 5. Clarendon press Oxford.

Bockelée-Morvan, D., Debout, V., Erard, S., Leyrat, C., Capaccioni, F., Filacchione, G., Fougere, N., Drossart, P., Arnold, G., Combi, M., Schmitt, B., Crovisier, J., de Sanctis, M.-C., Encrenaz, T., Kührt, E., Palomba, E., Taylor, F.W., Tosi, F., Piccioni, G., Fink, U., Tozzi, G., Barucci, A., Biver, N., Capria, M.-T., Ip, W., Blecka, M., Henry, F., Jacquinod, S., Reess, J.-M., Semery, A., Tiphene, D., 2015. First observations of H2O and CO2 vapor in comet 67P/Churyumov-Gerasimenko made by VIRTIS onboard Rosetta. Astron. Astrophys. 583, A6.

Bohren, C.F., Huffman, D.R., 1983. Absorption and Scattering of Light by Small Particles. Wiley-Interscience, New York.

Burns, J.A., Lamy, P.L., Soter, S., 1979. Radiation forces on small particles in the solar system. Icarus 40, 1–48.

Combi, M.R., Harris, W.M., Smyth, W.H., 2004. Comets II. University of Arizona Press, pp. 523–552.

Combi, M., Shou, Y., Fougere, N., Tenishev, V., Altwegg, K., Rubin, M., Bockelée-Morvan, D., Capaccioni, F., Cheng, Y.-C., Fink, U., Gombosi, T., Hansen, K.C., Huang, Z., Marshall, D., Toth, G., 2020. The surface distributions of the production of the major volatile species, H2O, CO2, CO and O2, from the nucleus of comet 67P/Churyumov-Gerasimenko throughout the Rosetta Mission as measured by the ROSINA double focusing mass spectrometer. Icarus 335, 113421.

Combi, M.R., Tenishev, V.M., Rubin, M., Fougere, N., Gombosi, T.I., 2012. Narrow dust jets in a diffuse gas coma: a natural product of small active regions on comets. Astrophys. J. 749 (1), 29.

Coradini, A., Capaccioni, F., Drossart, P., Arnold, G., Ammannito, E., Angrilli, F., Barucci, A., Bellucci, G., Benkhoff, J., Bianchini, G., Bibring, J.P., Blecka, M., Bockelee-Morvan, D., Capria, M.T., Carlson, R., Carsenty, U., Cerroni, P., Colangeli, L., Combes, M., Combi, M., Crovisier, J., Desanctis, M.C., Encrenaz, E.T., Erard, S., Federico, C., Filacchione, G., Fink, U., Fonti, S., Formisano, V., Ip, W.H., Jauman, R., Kührt, E., Langevin, Y., Magni, G., Mccord, T., Mennella, V., Mottola, S., Neukum, G., Palumbo, P., Piccioni, G., Rauer, H., Saggin, B., Schmitt, B., Tiphene, D., Tozzi, G., 2007. Virtis: An imaging spectrometer for the rosetta mission. Space Sci. Rev. 128, 529–559.

Crifo, J.-F., Loukianov, G.A., Rodionov, A.V., Zakharov, V.V., 2005. Direct Monte Carlo and multifluid modeling of the circumnuclear dust coma: Spherical grain dynamics revisited. Icarus 176 (1), 192–219.

Fornasier, S., Hasselmann, P.H., Barucci, M.A., Feller, C., Besse, S., Leyrat, C., Lara, L., Gutierrez, P.J., Oklay, N., Tubiana, C., Scholten, F., Sierks, H., Barbieri, C., Lamy, P.L., Rodrigo, R., Koschny, D., Rickman, H., Keller, H.U., Agarwal, J., A´Hearn, M.F., Bertaux, J.-L., Bertini, I., Cremonese, G., Da Deppo, V., Davidsson, B., Debei, S., De Cecco, M., Fulle, M., Groussin, O., Güttler, C., Hviid, S.F., Ip, W., Jorda, L., Knollenberg, J., Kovacs, G., Kramm, R., Kührt, E., Küppers, M., La Forgia, F., Lazzarin, M., Lopez Moreno, J.J., Marzari, F., Matz, K.-D., Michalik, H., Moreno, F., Mottola, S., Naletto, G., Pajola, M., Pommerol, A., Preusker, F., Shi, X., Snodgrass, C., Thomas, N., Vincent, J.-B., 2015. Spectrophotometric properties of the nucleus of comet 67P/Churyumov-Gerasimenko from the OSIRIS instrument onboard the ROSETTA spacecraft. Astron. Astrophys. 583, A30.

Fougere, N., Altwegg, K., Berthelier, J.-J., Bieler, A., Bockelée-Morvan, D., Calmonte, U., Capaccioni, F., Combi, M.R., De Keyser, J., Debout, V., Erard, S., Fiethe, B., Filacchione, G., Fink, U., Fuselier, S.A., Gombosi, T.I., Hansen, K.C., Hässig, M., Huang, Z., Le Roy, L., Leyrat, C., Migliorini, A., Piccioni, G., Rinaldi, G., Rubin, M., Shou, Y., Tenishev, V., Toth, G., Tzou, C.-Y., and the VIRTIS and the ROSINA teams, 2016. Direct Simulation Monte Carlo modelling of the major species in the coma of comet 67P/Churyumov-Gerasimenko. Mon. Not. R. Astron. Soc. 462 (Suppl_1), S156–S169.

Fulle, M., Ivanovski, S.L., Bertini, I., Gutierrez, P., Lara, L., Sierks, H., Zakharov, V., Della Corte, V., Rotundi, A., Barbieri, C., Lamy, P.L., Rodrigo, R., Koschny, D., Rickman, H., Keller, H.U., Agarwal, J., A´Hearn, M.F., Barucci, M.A., Bertaux, J.-L., Bodewits, D., Cremonese, G., Da Deppo, V., Davidsson, B., Debei, S., De Cecco, M., Fornasier, S., Groussin, O., Güttler, C., Hviid, S.F., Ip, W., Jorda, L., Knollenberg, J., Kramm, R., Kührt, E., Küppers, M., Lazzarin, M., Lopez-Moreno, J.J., Marzari, F., Michalik, H., Naletto, G., Oklay, N., Sabau, L., Thomas, N., Tubiana, C., Vincent, J.-B., Wenzel, K.-P., 2015. Rotating dust particles in the coma of comet 67p/churyumov-gerasimenko. Astron. Astrophys. 583, A14.

Gerig, S.B., Marschall, R., Thomas, N., Bertini, I., Bodewits, D., Davidsson, B., Fulle, M., Ip, W.H., Keller, H.U., Küppers, M., Preusker, F., Scholten, F., Su, C.C., Toth, I., Tubiana, C., Wu, J.S., Sierks, H., Barbieri, C., Lamy, P.L., Rodrigo, R., Koschny, D., Rickman, H., Agarwal, J., Barucci, M.A., Bertaux, J.L., Cremonese, G., Da Deppo, V., Debei, S., De Cecco, M., Deller, J., Fornasier, S., Groussin, O., Gutierrez, P.J., Güttler, C., Hviid, S.F., Jorda, L., Knollenberg, J., Kramm, J.R., Kührt, E., Lara, L.M., Lazzarin, M., Lopez Moreno, J.J., Marzari, F., Mottola, S., Naletto, G., Oklay, N., Vincent, J.B., 2018. On deviations from free-radial outflow in the inner coma of comet 67P/Churyumov-Gerasimenko. Icarus 311, 1–22.

Groussin, O., Attree, N., Brouet, Y., Ciarletti, V., Davidsson, B., Filacchione, G., Fischer, H.-H., Gundlach, B., Knapmeyer, M., Knollenberg, J., Kokotanekova, R., Kührt, E., Leyrat, C., Marshall, D., Pelivan, I., Skorov, Y., Snodgrass, C., Spohn, T., Tosi, F., 2019. The thermal, mechanical, structural, and dielectric properties of cometary nuclei after rosetta. Space Sci. Rev. 215 (29).

Gulkis, S., Frerking, M., Crovisier, J., Beaudin, G., Hartogh, P., Encrenaz, P., Koch, T., Kahn, C., Salinas, Y., Nowicki, R., Irigoyen, R., Janssen, M., Stek, P., Hofstadter, M., Allen, M., Backus, C., Kamp, L., Jarchow, C., Steinmetz, E., Deschamps, A., Krieg, J., Gheudin, M., Bockelée-Morvan, D., Biver, N., Encrenaz, T., Despois, D., Ip, W., Lellouch, E., Mann, I., Muhleman, D., Rauer, H., Schloerb, P., Spilker, T., 2007. MIRO: Microwave instrument for rosetta orbiter. Space Sci. Rev. 128 (1), 561–597.

Hansen, K.C., Altwegg, K., Berthelier, J.J., Bieler, A., Biver, N., Bockelée-Morvan, D., Calmonte, U., Capaccioni, F., Combi, M.R., de Keyser, J., Fiethe, B., Fougere, N., Fuselier, S.A., Gasc, S., Gombosi, T.I., Huang, Z., Le Roy, L., Lee, S., Nilsson, H., Rubin, M., Shou, Y., Snodgrass, C., Tenishev, V., Toth, G., Tzou, C.Y., Wedlund, C.S., Team, R., 2016. Evolution of water production of 67P/Churyumov-Gerasimenko: An empirical model and a multi-instrument studyEvolution of water production of 67P/Churyumov-Gerasimenko: An empirical model and a multi-instrument study. Mon. Not. R. Astron. Soc. 462, 491–506.

Hapke, B., 1981. Bidirectional reflectance spectroscopy: 1. Theory. J. Geophys. Res. 86 (B4), 3039–3054.

Hapke, B., 1993. Theory of Reflectance and Emittance Spectroscopy. Cambridge University Press.

Hapke, B., 2002. Bidirectional reflectance spectroscopy. 5. The Coherent backscatter opposition effect and anisotropic scattering. Icarus 157 (2), 523–534.

Ho, T.-M., Thomas, N., Boice, D.C., Combi, M., Soderblom, L.A., Tenishev, V., 2007. Comparison of the dust distribution in the inner comae of comets - 1P/halley and 19P/Borrelly spacecraft observations. Planet. Space Sci. 55, 974–985.

Jorda, L., Gaskell, R., Capanna, C., Hviid, S., Lamy, P., Ďurech, J., Faury, G., Groussin, O., Gutiérrez, P., Jackman, C., Keihm, S.J., Keller, H.U., Knollenberg, J., Kührt, E., Marchi, S., Mottola, S., Palmer, E., Schloerb, F.P., Sierks, H., Vincent, J.-B., A'Hearn, M.F., Barbieri, C., Rodrigo, R., Koschny, D., Rickman, H., Barucci, M.A., Bertaux, J.L., Bertini, I., Cremonese, G., Da Deppo, V., Davidsson, B., Debei, S., De Cecco, M., Fornasier, S., Fulle, M., Güttler, C., Ip, W.-H., Kramm, J.R., Küppers, M., Lara, L.M., Lazzarin, M., Lopez Moreno, J.J., Marzari, F., Naletto, G., Oklay, N., Thomas, N., Tubiana, C., Wenzel, K.-P., 2016. The global shape, density and rotation of Comet 67P/Churyumov-Gerasimenko from preperihelion Rosetta/OSIRIS observations. Icarus 277, 257–278.

Keller, H.U., Barbieri, C., Lamy, P., Rickman, H., Rodrigo, R., Wenzel, K.-P., Sierks, H., A'Hearn, M.F., Angrilli, F., Angulo, M., Bailey, M.E., Barthol, P., Barucci, M.A., Bertaux, J.-L., Bianchini, G., Boit, J.-L., Brown, V., Burns, J.A., Büttner, I., Castro, J.M., Cremonese, G., Curdt, W., da Deppo, V., Debei, S., de Cecco, M., Dohlen, K., Fornasier, S., Fulle, M., Germerott, D., Gliem, F., Guizzo, G.P., Hviid, S.F., Ip, W.-H., Jorda, L., Koschny, D., Kramm, J.R., Kührt, E., Küppers, M., Lara, L.M., Llebaria, A., López, A., López-Jimenez, A., López-Moreno, J., Meller, R., Michalik, H., Michelena, M.D., Müller, R., Naletto, G., Origné, A., Parzianello, G., Pertile, M., Quintana, C., Ragazzoni, R., Ramous, P., Reiche, K.-U., Reina, M., Rodríguez, J., Rousset, G., Sabau, L., Sanz, A., Sivan, J.-P., Stöckner, K., Tabero, J., Telljohann, U., Thomas, N., Timon, V., Tomasch, G., Wittrock, T., Zaccariotto, M., 2007. OSIRIS the scientific camera system Onboard Rosetta. Space Sci. Rev. 128, 433–506.

Keller, H.U., Thomas, N., 1989. Evidence for near-surface breezes on comet P/Halley. Astron. Astrophys. 226, L9–L12.

King, M.D.K., Greenstone, R. (Eds.), 1999. 1999 EOS Reference Handbook: A guide to NASA's Earth Science Enterprise and the Earth Observing System. NASA/Goddard Space Flight Center, (https://eospso.gsfc.nasa.gov/publications/56).

Kissel, J., Altwegg, K., Clark, B.C., Colangeli, L., Cottin, H., Czempiel, S., Eibl, J., Engrand, C., Fehringer, H.M., Feuerbacher, B., Fomenkova, M., Glasmachers, A., Greenberg, J.M., Grün, E., Haerendel, G., Henkel, H., Hilchenbach, M., von Hoerner, H., Höfner, H., Hornung, K., Jessberger, E.K., Koch, A., Krüger, H., Langevin, Y., Parigger, P., Raulin, F., Rüdenauer, F., Rynö, J., Schmid, E.R.,

Schulz, R., Silén, J., Steiger, W., Stephan, T., Thirkell, L., Thomas, R., Torkar, K., Utterback, N.G., Varmuza, K., Wanczek, K.P., Werther, W., Zscheeg, H., 2007. Cosima high resolution time-of-flight secondary ion mass spectrometer for the analysis of cometary dust particles onboard rosetta. Space Sci. Rev. 128, 823–867.

Knollenberg, J., Lin, Z.Y., Hviid, S.F., Oklay, N., Vincent, J.-B., Bodewits, D., Mottola, S., Pajola, M., Sierks, H., Barbieri, C., Lamy, P., Rodrigo, R., Koschny, D., Rickman, H., A'Hearn, M.F.A., Barucci, M.A., Bertaux, J.L., Bertini, I., Cremonese, G., Davidsson, B., Da Deppo, V., Debei, S., De Cecco, M., Fornasier, S., Fulle, M., Groussin, O., Gutiérrez, P.J., Ip, W.-H., Jorda, L., Keller, H.U., Kührt, E., Kramm, J.R., Küppers, M., Lara, L.M., Lazzarin, M., Lopez Moreno, J.J., Marzari, F., Naletto, G., Thomas, N., Güttler, C., Preusker, F., Scholten, F., Tubiana, C., 2016. A mini outburst from the nightside of comet 67p/churyumov-gerasimenko observed by the osiris camera on rosetta. Astron. Astrophys. 596, A89.

Le Roy, L., Altwegg, K., Balsiger, H., Berthelier, J.-J., Bieler, A., Briois, C., Calmonte, U., Combi, M.R., De Keyser, J., Dhooghe, F., Fiethe, B., Fuselier, S.A., Gasc, S., Gombosi, T.I., Hässig, M., Jäckel, A., Rubin, M., Tzou, C.-Y., 2015. Inventory of the volatiles on comet 67p/churyumov-gerasimenko from rosetta/rosina. Astron. Astrophys. 583, A1.

Marschall, R., 2017. Inner Gas and Dust Comae of Comets - Building a 3D Simulation Pipeline to Understand Multi-Instrument Results from the Rosetta Mission to Comet 67P/Churyumov-Gerasimenko (Ph.D. thesis). University of Bern.

Marschall, R., Mottola, S., Su, C.C., Liao, Y., Rubin, M., Wu, J.S., Thomas, N., Altwegg, K., Sierks, H., Ip, W.-H., Keller, H.U., Knollenberg, J., Kührt, E., Lai, I.L., Skorov, Y., Jorda, L., Preusker, F., Scholten, F., Vincent, J.-B., Team, O., Team, R., 2017. Cliffs versus plains: Can ROSINA/COPS and OSIRIS data of comet 67P/Churyumov-Gerasimenko in autumn 2014 constrain inhomogeneous outgassing?. Astron. Astrophys. 605, A112.

Marschall, R., Rezac, L., Kappel, D., Su, C.C., Gerig, S.-B., Rubin, M., Pinzón-Rodríguez, O., Marshall, D., Liao, Y., Herny, C., Arnold, G., Christou, C., Dadzie, S.K., Groussin, O., Hartogh, P., Jorda, L., Kührt, E., Mottola, S., Mousis, O., Preusker, F., Scholten, F., Theologou, P., Wu, J.-S., Altwegg, K., Rodrigo, R., Thomas, N., 2019. A comparison of multiple rosetta data sets and 3D model calculations of 67P/Churyumov-Gerasimenko coma around equinox (May 2015). Icarus 328, 104–126.

Marschall, R., Su, C.C., Liao, Y., Thomas, N., Altwegg, K., Sierks, H., Ip, W.-H., Keller, H.U., 2016. Modelling observations of the inner gas and dust coma of comet 67P/Churyumov-Gerasimenko using ROSINA/COPS and OSIRIS data: First results. Astron. Astrophys. 589, A90.

Marshall, D., Groussin, O., Vincent, J.-B., Brouet, Y., Kappel, D., Arnold, G., Capria, M.T., Filacchione, G., Hartogh, P., Hofstadter, M., Ip, W.-H., Jorda, L., Kührt, E., Lellouch, E., Mottola, S., Rezac, L., Rodrigo, R., Rodionov, S., Schloerb, P., Thomas, N., 2018. Thermal inertia and roughness of the nucleus of comet 67P/Churyumov-Gerasimenko from MIRO and VIRTIS observations. Astron. Astrophys. 616, A122.

Merouane, S., Stenzel, O., Hilchenbach, M., Schulz, R., Altobelli, N., Fischer, H., Hornung, K., Kissel, J., Langevin, Y., Mellado, E., Rynö, J., Zaprudin, B., 2017. Evolution of the physical properties of dust and cometary dust activity from 67P/Churyumov–Gerasimenko measured in situ by Rosetta/COSIMA. Mon. Not. R. Astron. Soc. 469 (Suppl_2), 459–474.

Pätzold, M., Andert, T.P., Hahn, M., Barriot, J.-P., Asmar, S.W., Häusler, B., Bird, M.K., Tellmann, S., Oschlisniok, J., Peter, K., 2018. The Nucleus of comet 67P/Churyumov–Gerasimenko – Part I: The global view – nucleus mass, mass-loss, porosity, and implications. Mon. Not. R. Astron. Soc. 483 (2), 2337–2346.

Pommerol, A., Thomas, N., El-Maarry, M.R., Pajola, M., Groussin, O., Auger, A.-T., Oklay, N., Fornasier, S., Feller, C., Davidsson, B., Gracia-Berná, A., Jost, B., Marschall, R., Poch, O., Barucci, M.A., Bertaux, J.-L., La Forgia, F., Keller, H.U., Kührt, E., Lowry, S.C., Mottola, S., Naletto, G., Sierks, H., Barbieri, C., Lamy, P.L., Rodrigo, R., Koschny, D., Rickman, H., Agarwal, J., A´Hearn, M.F., Bertini, I., Boudreault, S., Cremonese, G., Da Deppo, V., De Cecco, M., Debei, S., Güttler, C., Fulle, M., Gutierrez, P.J., Hviid, S.F., Ip, W.-H., Jorda, L., Knollenberg, J., Kovacs, G., Kramm, J.-R., Küppers, E., Lara, L., Lazzarin, M., Lopez Moreno, J.L., Marzari, F., Michalik, H., Preusker, F., Scholten, F., Tubiana, C., Vincent, J.-B., 2015. OSIRIS observations of meter-sized exposures of H2O ice at the surface of 67P/Churyumov-Gerasimenko and interpretation using laboratory experiments. Astron. Astrophys. 583, A25.

Preusker, F., Scholten, F., Matz, K.-D., Roatsch, T., Hviid, S.F., Mottola, S., Knollenberg, J., Kührt, E., Pajola, M., Oklay, N., Vincent, J.-B., Davidsson, B., A'Hearn, M.F., Agarwal, J., Barbieri, C., Barucci, M.A., Bertaux, J.-L., Bertini, I., Cremonese, G., Da Deppo, V., Debei, S., De Cecco, M., Fornasier, S., Fulle, M., Groussin, O., Gutiérrez, P.J., Güttler, C., Ip, W.-H., Jorda, L., Keller, H.U., Koschny, D., Kramm, J.R., Küppers, M., Lamy, P., Lara, L.M., Lazzarin, M., Lopez Moreno, J.J., Marzari, F., Massironi, M., Naletto, G., Rickman, H., Rodrigo, R., Sierks, H., Thomas, N., Tubiana, C., 2017. The global meter-level shape model of comet 67P/Churyumov-Gerasimenko. Astron. Astrophys. 607, L1.

Rinaldi, G., Fink, U., Doose, L., Tozzi, G.P., Capaccioni, F., Filacchione, G., Bockelée-Morvan, D., Leyrat, C., Piccioni, G., Erard, S., Bieler, A., Blecka, M., Ciarniello, M., Combi, M., Fougere, N., Migliorini, E., Palomba, A., Raponi, A., Taylor, F., 2016. Properties of the dust in the coma of 67p/churyumov-gerasimenko observed with virtis-m. Mon. Not. R. Astron. Soc. 462, 547–561.

Rinaldi, G., Formisano, M., Kappel, D., Capaccioni, F., Bockelée-Morvan, D., Cheng, Y.-C., Vincent, J.-B., Deshapriya, P., Arnold, G., Capria, M.T., Ciarniello, M., D'Aversa, E.D., De Sanctis, M.C., Doose, L., Erard, S., Federico, C., Filacchione, G., Fink, U., Leyrat, C., Longobardo, A., Magni, G., Migliorini, A., Mottola, S., Naletto, G., Raponi, A., Taylor, F., Tosi, F., Tozzi, G.P., Salatti, M., 2019. Analysis of night-side dust activity on comet 67p observed by virtis-m: a new method to constrain the thermal inertia on the surface. Astron. Astrophys. 630, A21.

Schloerb, F.P., Keihm, S., von Allmen, P., Choukroun, M., Lellouch, E., Leyrat, C., Beaudin, G., Biver, N., Bockelée-Morvan, D., Crovisier, J., Encrenaz, P., Gaskell, R., Gulkis, S., Hartogh, P., Hofstadter, M., Ip, W.-H., Janssen, M., Jarchow, C., Jorda, L., Keller, H.U., Lee, S., Rezac, L., Sierks, H., 2015. MIRO observations of subsurface temperatures of the nucleus of 67P/Churyumov-Gerasimenko. Astron. Astrophys. 583, A29.

Shi, X., Hu, X., Sierks, H., Güttler, C., A'Hearn, M., Blum, J., El-Maarry, M.R., Kührt, E., Mottola, S., Pajola, M., Oklay, N., Fornasier, S., Tubiana, C., Keller, H., Vincent, J.-B., Bodewits, D., Höfner, S., Lin, Z.-Y., Gicquel, A., Hofmann, M., Barbieri, C., Lamy, P.L., Rodrigo, R., Koschny, D., Rickman, H., Barucci, M.A., Bertaux, J.-L., Bertini, I., Cremonese, G., Da Deppo, V., Davidsson, B., Debei, S., De Cecco, M., Fulle, M., Groussin, O., Gutiérrez, P.J., Hviid, S.F., Ip, W.-H., Jorda, L., Knollenberg, J., Kovacs, G., J.-R., K., Küppers, M., Lara, L.M., Lazzarin, M., Lopez-Moreno, J.J., Marzari, F., Naletto, G., Thomas, N., 2016. Sunset jets observed on comet 67p/churyumov-gerasimenko sustained by subsurface thermal lag. Astron. Astrophys. 586, A7.

Spohn, T., Knollenberg, J., Ball, A.J., Banaszkiewicz, M., Benkhoff, J., Grott, M., Grygorczuk, J., Hüttig, C., Hagermann, A., Kargl, G., Kaufmann, E., Kömle, N., Kührt, E., Kossacki, K.J., Marczewski, W., Pelivan, I., Schrödter, R., Seiferlin, K., 2015. Thermal and mechanical properties of the near-surface layers of comet 67P/Churyumov-Gerasimenko. Science 349 (6247).

Su, C.C., 2013. Parallel Direct Simulation Monte Carlo (DSMC) Methods for Model- ing Rarefied Gas Dynamics (Ph.D. thesis). National Chiao Tung University, Taiwan.

Tenishev, V., Combi, M.R., Rubin, M., 2011. Numerical simulation of dust in a cometary coma: Application to comet 67P/Churyumov-Gerasimenko. Astrophys. J. 732 (2), 104.

Thomas, N., Keller, H., 1990. Interpretation of the inner coma observations of comet P/Halley by Halley Multicolour Camera. Ann. Geophys. 8, 147–166.

Thomas, N., Sierks, H., Barbieri, C., Lamy, P.L., Rodrigo, R., Rickman, H., Koschny, D., Keller, H.U., Agarwal, J., A'Hearn, M.F., Angrilli, F., Auger, A.-T., Barucci, M.A., Bertaux, J.-L., Bertini, I., Besse, S., Bodewits, D., Cremonese, G., Da Deppo, V., Davidsson, B., De Cecco, M., Debei, S., El-Maarry, M.R., Ferri, F., Fornasier, S., Fulle, M., Giacomini, L., Groussin, O., Gutierrez, P.J., Güttler, C., Hviid, S.F., Ip, W.-H., Jorda, L., Knollenberg, J., Kramm, J.-R., Kührt, E., Küppers, M., La Forgia, F., Lara, L.M., Lazzarin, M., Moreno, J.J.L., Magrin, S., Marchi, S., Marzari, F., Massironi, M., Michalik, H., Moissl, R., Mottola, S., Naletto, G., Oklay, N., Pajola, M., Pommerol, A., Preusker, F., Sabau, L., Scholten, F., Snodgrass, C., Tubiana, C., Vincent, J.-B., Wenzel, K.-P., 2015. The morphological diversity of comet 67P/Churyumov-Gerasimenko. Science 347 (1).

Tubiana, C., Güttler, C., Kovacs, G., Bertini, I., Bodewits, D., Fornasier, S., Lara, L., La Forgia, F., Magrin, S., Pajola, M., Sierks, H., Barbieri, C., Lam, P.L., Rodrigo, R., Koschny, D., Rickman, H., Keller, H.U., Agarwal, J., A'Hearn, M.F., Barucci, M.A., Bertaux, J.-L., Besse, S., Boudreault, S., Cremonese, G., Da Deppo, V., Davidsson, B., Debei, S., De Cecco, M., El-Maarry, M.R., Fulle, M., Groussin, O., Gutiérrez-Marques, P., Gutiérrez, P.J., Hoekzema, N., Hofmann, M., Hviid, S.F., Ip, W.-H., Jorda, L., Knollenberg, J., Kramm, J.-R., Kührt, E., Küppers, M., Lazzarin, M., Lopez Moreno, J.J., Marzari, F., Massironi, M., Michalik, H., Moissl, R., Naletto, G., Oklay, N., Scholten, F., Shi, X., Thomas, N., Vincent, J.-B., 2015. Scientific assessment of the quality of OSIRIS images. Astron. Astrophys. 583, A46.

Tubiana, C., Rinaldi, G., Güttler, C., Snodgrass, C., Shi, X., Hu, X., Marschall, R., Fulle, M., Bockelée-Morvan, D., Naletto, G., Capaccioni, F., Sierks, H., Arnold, G., Barucci, M.A., Bertaux, J.-L., Bertini, I., Bodewits, D., Capria, M.T., Ciarniello, M., Cremonese, G., Crovisier, J., Da Deppo, V., Debei, S., De Cecco, M., Deller, J., De Sanctis, M.C., Davidsson, B., Doose, L., Erard, S., Filacchione, G., Fink, U., Formisano, M., Fornasier, S., Gutiérrez, P.J., Ip, W.-H., Ivanovski, S., Kappel, D., Keller, H.U., Kolokolova, L., Koschny, D., Krueger, H., La Forgia, F., Lamy, P.L., Lara, L.M., Lazzarin, M., Lavasseur-Regourd, A.C., Lin, Z.-Y., Longobardo, A., López-Moreno, J.J., Marzari, F., Migliorini, A., Mottola, S., Rodrigo, R., Taylor, F., Toth, I., Zakharov, V., 2019. Diurnal variations of dust and gas production in comet 67p/churyumov-gerasimenko at the inbound equinox as seen by osiris and virtis-m on board rosetta. Astron. Astrophys. 630, A23.

Wu, J.-S., Lian, Y.-Y., 2003. Parallel three-dimensional direct simulation Monte Carlo method and its applications. Comput. & Fluids 32 (Issue 8), 1133–1160.

Wu, J.-S., Tseng, K.-C., 2005. Parallel DSMC method using dynamic domain decomposition. Internat. J. Numer. Methods Engrg. 63, 37–76.

Wu, J.-S., Tseng, K.-C., Wu, F.-Y., 2004. Parallel tree-dimensional Dsmc method using mesh refinement and variable time-step scheme. Comput. Phys. Comm. 162, 166–187.

Zakharov, V.V., Crifo, J.-F., Rodionov, A., Rubin, M., Altwegg, K., 2018a. The near-nucleus gas coma of comet 67P/Churyumov-Gerasimenko prior to the descent of the surface lander PHILAE. Astron. Astrophys. 618, A71.

Zakharov, V.V., Ivanovski, S.L., Crifo, J.-F., Della Corte, V., Rotundi, A., Fulle, M., 2018b. Asymptotics for spherical particle motion in a spherically expanding flow. Icarus 312, 121–127.